



Unraveling the Spectral Energy Distributions of Clustered YSOs

J. Rafael Martínez-Galarza¹ , Pavlos Protopapas², Howard A. Smith¹, and Esteban F. E. Morales³

¹Harvard-Smithsonian Center for Astrophysics, 60 Garden Street, Cambridge, MA 02138, USA; jmartine@cfa.harvard.edu
²Institute for Applied Computational Science, Harvard University, Northwest B162, 52 Oxford Street, Cambridge, MA 02138, USA
³I. Physikalisches Institut Universität zu Köln Zùlpicherstr. 77 50937 Köln, Germany

Received 2018 February 14; revised 2018 July 3; accepted 2018 July 18; published 2018 August 30

Abstract

Despite significant evidence suggesting that intermediate- and high-mass stars form in clustered environments, how stars form when the available resources are shared is still not well understood. A related question is whether the initial mass function (IMF) is in fact universal across galactic environments, or whether it is an average of IMFs that differ, for example, in massive versus low-mass molecular clouds. One of the long-standing problems in resolving these questions and in the study of young clusters is observational: how to accurately combine multiwavelength data sets obtained using telescopes with different spatial resolutions. The resulting confusion hinders our ability to fully characterize clustered star formation. Here we present a new method that uses Bayesian inference to fit the blended spectral energy distributions and images of *individual* young stellar objects (YSOs) in confused clusters. We apply this method to the infrared photometry of a sample comprising 70 *Spitzer*-selected, low-mass ($M_{cl} < 100 M_{\odot}$) young clusters in the galactic plane, and we use the derived physical parameters to investigate how the distribution of YSO masses within each cluster relates to the total mass of the cluster. We find that for low-mass clusters this distribution is indistinguishable from a randomly sampled Kroupa IMF for this range of cluster masses. Therefore, any effects of self-regulated star formation that affect the IMF sampling are likely to play a role only at larger cluster masses. Our results are also compatible with smoothed particle hydrodynamics models that predict a dynamical termination of the accretion in protostars, with massive stars undergoing this stopping at later times in their evolution.

Key words: methods: statistical – open clusters and associations: general – stars: formation – stars: protostars – stars: statistics

1. Introduction

The physical characterization of individual young stars at different stages of their formation, from an initial cold clump that undergoes gravitational collapse to the onset of the hydrogen-burning phase and through a period of gas accretion that can last for several million years, is at the base of our understanding of the process of star formation at global scales. Key outstanding questions relate to the initial mass function (IMF): are all of the stellar masses in the galaxy produced via a single universal IMF, or does the distribution of masses depend on the environment, making the integrated galactic IMF of stars (IGIMF; Kroupa & Weidner 2003) different from the canonical IMF? If it depends on environment, how different can it be, and why? The answers to these questions are intimately linked to the processes of early star formation and the universality of the IMF (Kroupa 2001; Kroupa & Boily 2002; Chabrier 2003; Elmegreen et al. 2008; Bastian et al. 2010; Kroupa et al. 2013).

If the IMF results from a random sampling process in any given cluster, then star formation is agnostic to the conditions of the environment, including the total mass of the birth cluster; no self-regulation is at play (other than setting a limit to the maximum stellar mass if the entire cluster mass resides in that star). Alternatively, the stellar masses in a cluster are preferentially determined by some kind of feedback (for example, competitive accretion), starting with the most massive of its members in such a way the resulting IGIMF has no gaps. This self-regulated process results in optimal sampling (Kroupa et al. 2013) and populates the cluster with an optimal number of stars starting from the most massive star in the cluster. Self-regulated star formation implies that the mass of the most massive star should depend on the available resources in the

cluster, and that there should exist a nontrivial correlation between the stellar mass of the cluster (M_{cl}) and the mass of its most massive star (m_{max}). While the existence of a correlation is not unique to self-regulation, other models of star formation predict a correlation with distinctly different slopes and cutoffs.

Stellar clusters provide a valuable resource in probing the answers to such questions about the shape and cutoff of the IMF because their populations reflect the distribution of stellar masses possible in a range of cluster masses, and hence the extent to which these environmental effects influence the stellar mass distribution. Observational properties of clusters also allow for critical comparisons between existing models. In the competitive accretion scenario (Bonnell et al. 2001), for example, stars in a young cluster accrete from a shared reservoir of gas, and in the cluster core the high relative velocities between stars result in Bondi–Hoyle accretion that in turn produces a fragmented IMF that is steeper at the high-mass end. Not all models of star formation result in optimal sampling of an IMF: if star formation is not self-regulated, the IMF can be understood as a probability distribution, and stellar masses are randomly sampled from it (Weidner et al. 2013).

The preferred way to analyze clusters of young stars and characterize their stellar mass distributions is through multiwavelength surveys, especially in the infrared. Surveys of the galactic plane in the past decade, using the *Spitzer*, *Herschel*, and *WISE* observatories, have greatly improved the number statistics of individual observations. The analysis of these data sets to date has resulted in a scenario that generally agrees with early studies that suggested that a large fraction of stars form in embedded clusters (e.g., Lada & Lada 2003). The observations also revealed a continuous distribution of young stellar surface

densities in the galactic plane (Bressert et al. 2010), suggesting that there is no clear-cut distinction between isolated and clustered star formation but rather a broad range of environments forming stars. In addition to core clustering developing during the collapse and fragmentation of a massive primordial molecular cloud, a multiplicity of young stars is expected to develop at smaller scales when the conditions for disk fragmentation are met, as has been demonstrated by numerical simulations (Stamatellos & Whitworth 2009; Lomax et al. 2015) and observations (Tobin et al. 2016).

In this paper, we take a new approach to the issue of determining stellar masses in clusters using spectral energy distribution (SED) fitting. SED models are often applied to photometric data sets taken across optical and infrared bands, without taking into account unresolved multiplicity. Even for nearby clusters, where we have good chances of resolving individual young stellar objects (YSOs) at the shortest infrared wavelengths, the emission from individual stars is often blended together within the beam of infrared telescopes at longer wavelengths. So far, some of the most sophisticated attempts to address this problem involve replacing photometric bands with spatially resolved spectrophotometric points (Forbrich et al. 2010) and including bands in the fitting only as upper limits if there is evidence for multiplicity (Mottram et al. 2011). The Robitaille et al. (2006; R06 hereafter) SED models are by far the most common set of models used to characterize YSOs. They have been used to study the properties of entire star-forming regions both within the Milky Way (e.g., Indebetouw et al. 2007; Azimlu et al. 2015) and in the nearby Magellanic clouds (e.g., Simon et al. 2007; Carlson et al. 2012). However, it is almost always assumed that the modeled photometry comes from a single YSO (Robitaille 2008).

In order to deal with the issue of SED fitting of multiple YSOs, in this paper we propose a new method. We use existing SED models to create informative priors for the photometry of unresolved multiple systems, and we then perform Bayesian inference to obtain the most likely physical parameters of *individual* YSOs, given the set of images and blended photometry of the clusters. We apply this method to the SEDs of 70 low-mass ($M_{\text{cl}} < 100 M_{\odot}$), blended clusters. We interpret the derived physical parameters in the context of different models of star formation, and we discuss the implications of our results for the IMF in the mass range of these observations, which corresponds to the low-mass end of the cluster mass distribution. Our method is an alternative to recent methods that use hydrodynamical simulations to generate SEDs of multiple YSO systems, which can be computationally expensive (Lomax & Whitworth 2018).

This paper is organized as follows. In Section 2 we describe the photometry used in the present study, the determination of distances to the sources, and the matching technique used to associate multiple UKIRT InfraRed Deep Sky Survey (UKIDSS) sources to single Galactic Legacy Infrared Midplane Survey Extraordinaire (GLIMPSE) detections. Section 3 describes the probabilistic algorithm to simultaneously fit the SEDs and images of blended YSOs. We describe the results of applying this algorithm to the 70 clusters in Section 4, where we also describe the overall statistics of the SED parameters estimated with our method. In Section 5 we discuss the implications of our results for the sampling of the IMF in the mass range of the studied clusters and compare the correlations found between individual YSOs and their parent clusters with

theoretical and semiempirical models of star formation. Finally, in Section 6 we present our conclusions.

2. Observational Data Sets

We use observations from the GLIMPSE (Benjamin et al. 2003; Churchwell et al. 2009) and MIPS Inner Galactic Plane Survey (MIPSGAL; Carey et al. 2005) surveys, carried out with the *Spitzer Space Telescope's* InfraRed Array Camera (IRAC; Fazio et al. 2004) using bands IRAC 1 (3.6 μm), IRAC 2 (4.5 μm), IRAC 3 (5.6 μm), and IRAC 4 (8.0 μm). The data set of observations studied here covers the inner Galactic plane ($|\ell| \leq 65^\circ$). A first attempt to isolate intrinsically red sources from the large (>30 million sources) GLIMPSE catalog was made by Robitaille et al. (2008). They established several criteria to come up with a photometrically reliable set of red $\sim 2 \times 10^4$ sources that was not affected by saturation, sensitivity issues, or variability. In their catalog, which is at least 65% complete and consists of $\sim 19,000$ sources, approximately 30%–50% are likely to be AGB stars, and approximately 50%–70% are likely to be YSOs. The authors point out that their catalog does not provide a complete picture of Galactic star formation as seen by *Spitzer*, since it does not include blended sources, extended sources, or sources with molecular emission that blueshifts them in the IRAC bands.

Morales & Robitaille (2017; MR17 hereafter) have isolated a sample of 8325 GLIMPSE YSO candidates that have corresponding UKIDSS (Hewett et al. 2006) coverage. UKIDSS provides imaging data in the near-infrared (NIR) bands *J* (1.17 μm), *H* (1.49 μm), and *K* (2.03 μm) and has a better angular resolution than that of GLIMPSE by a factor >2 . In this paper, we are assuming that the sources detected in UKIDSS are resolved into individual objects, which we find a reasonable assumption at the range of heliocentric distances considered here. The UKIRT telescope resolution is characterized by 0.8 arcsec in the *J*, *H*, and *K* bands. At this resolution and given our range of heliocentric distances (~ 0.5 –15 kpc), we can resolve projected physical distances between 0.001 and 0.06 pc, whereas the typical separation between stars in a globular cluster is about 0.3 pc.

Following the MR17 approach, we use an empirical method for source matching that evaluates the smoothness of the SED transition between NIR and mid-infrared (MIR) bands for each of the UKIDSS sources with respect to the GLIMPSE/MIPSGAL fluxes by comparing the cubic spline that fits the SED of each UKIDSS source (and associated GLIMPSE/MIPSGAL source) with the simple quadratic function that fits the four middle points that define the NIR-to-MIR transition (*H*, *K*, 3.6, and 4.5 μm). Similarity between these two curves indicates a higher likelihood that a given UKIDSS source contributes to the GLIMPSE flux. This is a generic method that could be robustly applied for matching SEDs across gaps at other wavelengths.

We use the same quantitative criteria as MR17 (their Equation (2)) to identify UKIDSS sources that match the SED of the corresponding GLIMPSE object, but here we increase the angular distance threshold to $1''$ in order not to miss likely multiple matching UKIDSS sources that could be farther from the GLIMPSE object than the stricter original threshold of $0''.57$. We further expand this distance to $2''$ to account for marginal sources that might not match the SED according to the spline method, but that are potential contributors to the

IRAC fluxes. After manually discarding a few targets with extended emission for which the point spread function (PSF)-fitting photometry erroneously assigns multiple UKIDSS sources, we ended up with a sample of 194 GLIMPSE objects with more than one UKIDSS source contributing to the flux in the IRAC and MIPS bands, where they appear blended into a single source.

The above classification is equivalent to the one defined by MR17 as UM_SM (i.e., we also required that the K -band fluxes of the multiple UKIDSS sources were within a factor of 10), for which they found the greatest number of objects with cluster-like appearance in the UKIDSS images. The larger angular distance threshold used here, together with the visual refinement, allowed us to spot an important fraction of the ~ 265 UM_SM objects predicted by MR17 via Monte Carlo (MC) simulations of possible misclassification by the original SED matching criteria (with threshold of $0''.57$). The direct classification by MR17 (i.e., without MC simulations) gives only 79 objects within the UM_SM category.

We remark that this empirical SED matching only represents a preliminary step for cluster identification, and that the detailed cluster characterization done in the present paper does not adopt any assumption on the UKIDSS sources from that step. Indeed, all UKIDSS sources within $2''$ (corresponding to the width of the IRAC PSF) will be modeled here as potential contributors to the IRAC/MIPS fluxes. Therefore, in the context of this paper, we define a cluster as a single GLIMPSE source that has two or more matching UKIDSS sources within the radius defined by the IRAC PSF width, which is $2''$. We realize that this definition relies purely on spatial coincidence, and therefore we are not claiming that these objects are clusters in a dynamical or evolutionary sense. However, we believe that it is safe to assume that infrared sources that are close to each other and that have potentially matching SEDs belong to the same class and are likely to be physically related to each other. This assumption might be wrong in a few specific cases, but it is very unlikely that it will affect the validity of our statistical analysis.

We also note that, given that our selection represents a subset of the original catalog of YSO candidates identified by Robitaille et al. (2008) as single GLIMPSE sources, there are no objects in our sample that were already multiple in GLIMPSE. Figure 1 shows multiwavelength views for three of the selected clusters. Shown in the figure are three color images using both UKIDSS and IRAC colors, together with the SEDs in each case derived from the images.

Our final list of 70 low-mass YSO clusters (see Table 2) results from restricting the sample to those objects with available distance estimates, needed for the physical modeling performed in this paper. For objects that are part of a star-forming region (infrared dark cloud, submillimeter clump, H II region), we use the distances to the regions reported in the literature. For objects with LSR velocity measurements, we use a kinematic distance solution based on a Galactic rotation model following Morales et al. (2013, their Appendix B.4). For many other objects in our sample, we use the large data set of LSR velocities and kinematic distance ambiguity (KDA) resolutions provided by Wienen et al. (2015), who carried out molecular line follow-up observations toward several sources detected in the APEX Telescope Large Area Survey of the Galaxy (ATLASGAL).

3. Bayesian Parameter Estimation

This section describes the Bayesian parameter estimation methods that we have designed to characterize clustered YSOs.⁴ The statistical model for SED fitting is introduced first, followed by a discussion of the optimization and sampling of the resulting posterior probability distributions. The statistical model for image fitting is described at the end of the section, together with the strategy to combine results from SED and image fitting to reduce the variance of our results.

3.1. Likelihood

Our goal is to simultaneously fit the SEDs of m sources that are observed in n different bands. The sources appear resolved as individual objects in the first n' bands, but are blended together within the beams of the remaining $n-n'$ bands. Thus, in the unresolved bands, we have a single photometric measurement for all m sources. We fit the sources using a grid of precalculated model SEDs M that depend on parameters $\{\theta\}$. For source i , then, we have a set $\{\theta_i\}$ of parameters, and we can denote the full set of parameters for all sources $i = 1, \dots, m$ as $\Theta = \{\theta_1, \dots, \theta_m\}$. Data D consists of the fluxes observed in all bands, resolved and unresolved, and their respective uncertainties. For source i and resolved band j , the measured flux is F_{ij} , with associated measurement error σ_{ij} , whereas for the unresolved sources the integrated measured flux is F_j , with associated error σ_j . The modeled flux for source i in band j is M_{ij} . With this nomenclature, the log-likelihood of observing a particular set of photometry for the cluster, if we assume that it was drawn from model M , is

$$\log P(D|\Theta) \propto \frac{1}{n'} \sum_{j=1}^{n'} \left[- \sum_{i=1}^m \frac{(F_{ij} - M_{ij}(\Theta))^2}{2\sigma_{ij}^2} \right] - \frac{1}{n - n'} \sum_{j=n'+1}^n \frac{\left(F_j - \sum_{i=1}^m M_{ij}(\Theta) \right)^2}{2\sigma_j^2}. \quad (1)$$

Our problem reduces to finding the set of model parameters Θ that optimizes the probabilistic model above. We are therefore faced with a maximum-likelihood estimation problem. But rather than just finding the best-fitting model, we can use our predictive model to estimate the probabilities over all possible solutions; that is, we perform Bayesian inference.

3.2. Bayesian Formulation

Rather than being interested in knowing which observations are expected given the model parameters, we would like to infer the physics; that is, we want to know which parameter models are more probable given the observed photometry. This means that we assume the model parameters to be random variables with associated probability distributions $P(\Theta|D)$, as opposed to the frequentist view, in which parameters have absolute, true values. Once we infer $P(\Theta|D)$, the posterior distribution, we can obtain a point estimate for the parameter values, usually the maximum a posteriori (MAP) estimate. The marginalization of the joint posterior with respect to each model parameter also provides complete information about the uncertainties on those parameters. Formally, the chain rule

⁴ The Python code containing the detailed algorithms can be found at https://github.com/juramaga/Bayesian_fitter.

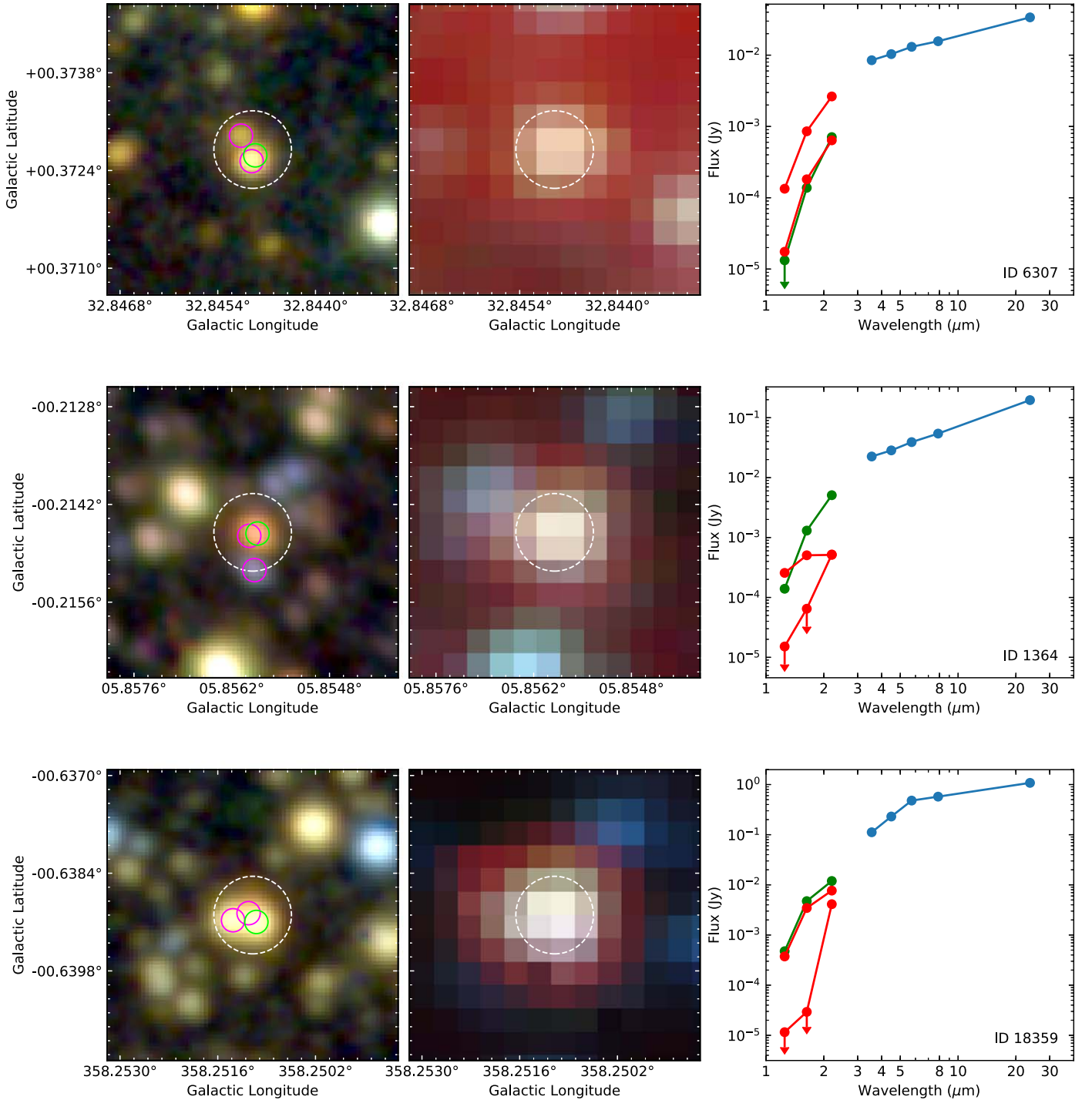


Figure 1. Three GLIMPSE sources with multiple UKIDSS matches. In each figure, the left panel is a composite three-color UKIDSS image with the *J* band in blue, the *H* band in green, and the *K* band in red, and the circles indicate the UKIDSS sources detected within $2''$ of the corresponding GLIMPSE source. The green circle is for the nearest source in angular separation, the magenta circles for the others, and the bigger dashed-line circle indicates the $2''$ search radius. The center panel is a composite three-color GLIMPSE image with the 3.6 μm band in blue, the 5.8 μm band in green, and the 8.0 μm band in red. The right panel shows the SEDs of the corresponding GLIMPSE (blue points) and UKIDSS sources (green points for the nearest source and red points for the others).

from probability theory provides a relation between the likelihood and the posterior distributions:

$$P(\Theta|D) \times P(D) = P(\Theta, D) = P(D|\Theta) \times P(\Theta), \quad (2)$$

which gives the well-known Bayes theorem:

$$P(\Theta|D) \propto P(D|\Theta)P(\Theta), \quad (3)$$

where $P(\Theta)$, the prior distribution, encodes any belief we might have (prior to obtaining the current photometry) on the parameter values. In general, priors become more informative in the analysis as fewer data points are available to inform the model.

The R06 models comprise a library of SED models for a broad range of YSO parameters. The fixed grid of parameter

values was originally generated by randomly sampling YSO ages (t) and masses (m_*), and then assigning corresponding accretion rates and disk/envelope properties using theoretical or semiempirical relations. The resulting SEDs (each of them generated at 10 different viewing angles) are then convolved with a library of observing filters from the ultraviolet to the far-infrared, giving model fluxes for all models in each band. To account for interstellar extinction, these “raw” SEDs can then be further obscured by a dust screen of optical extinction A_V , using the typical Galactic ISM extinction curve modified for the MIR extinction whose properties are derived in Indebetouw et al. (2005). The models are normalized to a distance of 1 kpc, but can be easily scaled to the desired distance.

The priors on mass (M_*) and age (t_*) are set by the original precalculated SED grid and are proper uniform priors $\mathcal{U}(\min, \max)$ defined on the logarithmic space of YSO ages and masses. Class 0 YSOs are undetected below $20 \mu\text{m}$, so we expect to detect mostly class I/II YSOs. The lifetime of a class I YSO is about 10^5 years, whereas that of a class II YSO is on average a few times 10^6 years. We modify the age prior and use a normal distribution $\mathcal{N}(\mu, \sigma)$ centered at $\log t_* = 5.5$ years with a broad standard deviation of one order of magnitude:

$$P(\log M_*) = \mathcal{U}(-1, 3) \quad (4)$$

$$P(\log t_*) = \mathcal{N}(5.5, \sigma = 1). \quad (5)$$

We use a normal prior for A_V . Although in principle we could use reddening data from Pan-STARSS photometry (e.g., Green et al. 2015) in order to obtain a better estimate of extinction in the line of sight and at the distance to our sources, we decide to adopt a more conservative approach: we use a normal distribution centered at $A_V = 10$ mag, with a standard deviation of $\sigma_{A_V} = 0.8$ mag. This mean is about 0.5 dex higher than the mean of the distribution for our sources, as derived from Pan-STARRS data, and is justified by the fact that at scales that are smaller than the beam of the 1.8 m Pan-STARRS telescope, we expect optical extinction to be higher than average toward regions of massive star formation. As for the inclination angle ϕ , we assume that it is proportional to the cosine of the inclination angle, as expected from an ensemble of randomly oriented disks:

$$P(\log A_V) = \mathcal{N}(1.0, \sigma = 0.8) \quad (6)$$

$$P(\phi) \propto \cos \phi. \quad (7)$$

We now have a probabilistic model that gives the posterior probability for the YSO parameters (Equation (3)). When computing $P(\Theta|D)$ by brute force, calculating the posterior at each possible point of the parameter space is computationally intractable. Even more so for the parameter space of our problem, whose dimensionality is $\dim = 4 \times n_{\text{sources}}$ (four parameters for each source plus one degree of freedom to account for uncertainty in the distance to the sources, minus one degree of freedom, due to the fact that the unresolved photometric points must satisfy the condition that their sum must equal the observed flux in each band).

The majority of the 14 varying parameters in the R06 models are correlated to other model parameters (Robitaille et al. 2006, 2008). For example, the envelope accretion rate (dM_{env}/dt) steeply decays for all models for ages beyond 10^5 years. In general, most parameters show a correlation with either the YSO mass or age. Therefore, for a cluster with three visible clustered YSOs (a typical case in our data set), the dimensionality of the

parameter space is 12, but dimensionality grows linearly with the number of sources. Typically, the three UKIDSS bands are observed for each of the cluster members, whereas the IRAC bands are observed for the cluster as a whole. The MIPS24 band is not available for all clusters. Therefore, for a cluster with three resolved UKIDSS sources, we have at most 14 observations available to fit the 12 parameters.

Probability distribution functions can be efficiently sampled using stochastic methods such as Markov chain Monte Carlo (MCMC) sampling. MCMC methods can be extremely slow at converging if the initial guess for the parameters is far from a significant peak of probability, especially in a parameter space with many dimensions, such as in our case. It is therefore a good course of action to first use an optimization algorithm to find a MAP estimate, and then use the MAP result to initialize the MCMC sampler.

3.3. Optimization of the Probabilistic Model with Genetic Algorithms

We use a genetic algorithm (GA) to optimize the posterior probability distribution prior to MCMC fitting. GAs are inspired in the stochasticity of biological evolution: given an initial population of solutions (we will call these solutions *individuals*), whose *genes* (the parameter values) are replicated using a particular mechanism into the following generation, only the fittest solutions (those with larger posterior probability) will survive after many generations. In the context of our problem, the fitness function is the posterior probability of Equation (3), and after each generation the resulting *population* will be graded according to the average value of this fitness. Given a random initial population, with random values assigned to the genes of each individual, at each generation we perform the following operations between individuals:

1. *Reproduction.* Given a population of individuals with different fitnesses, we update the population in such a way that the best-fit individuals will have more offspring, while keeping the total number of individuals unchanged.
2. *Crossover.* We randomly exchange genes between the members of the updated population to create new individuals. Such exchange of genes is performed by cutting and then exchanging parameters between parent individuals.
3. *Mutation.* Natural selection and diversity would not happen without unlikely random mutations of the genes. To simulate mutation in our population of individuals, we randomly change the value of one of the parameters in a random individual, with very low probability.

The average fitness of the new generation and the fitness of the individuals are evaluated. Evolution should lead to an increase in fitness with each generation. After a sufficient number of generations, the population should be primarily composed of highly fit individuals (i.e., solutions with a higher posterior probability). By selecting the best among these descendants, we obtain the best possible solution.

The main parameters controlling the outcome of this evolutionary process within the algorithm are as follows:

1. The size of the population (N). This parameter remains fixed along the entire simulation and should be adjusted so that it is not too small (which would make crossover

unlikely, resulting in only a small portion of the parameter space being explored) or too large (which would make the whole process very slow). We use a population of between 30 and 40 members, depending on the number of sources being fitted.

2. The probability of mutation (p_m), which should be kept low to avoid turning the algorithm into a random search. We have used values between 1% and 2%.
3. The survival rate of the best-fit individuals (p_s), that is, the fraction of individuals (ordered by decreasing fitness) that are selected to become parents of the next generation. Here we use between 20% and 40% for this parameter.
4. The probability p_o of an individual being selected to be a parent of the next generation even if they are not among the best-fit individuals. For this parameter we use a value of 5%.
5. The crossover probability (p_c), or how likely it is that crossover takes place. If there is no crossover at all, children are just identical copies of parents. Here we adopt $p_c = 1.0$.

Our adopted values represent a reasonable estimate based on trial-and-error experiments, and the final conclusions do not depend critically on their precise values. For each cluster in Table 2, we optimize the posterior probability of Equation (1) by applying the GA with the parameters specified above, over 10^4 generations, and we use the outcome of this process to initialize the MCMC fitting.

3.4. MCMC: Sampling the Parameter Posteriors

The output parameters of the GA optimization are used as initialization parameters of the MCMC sampler. We use our own implementation of the standard Metropolis–Hastings algorithm, for which we customize the proposal distributions in order for it to work with a discrete grid of model parameters. In the $t_* - M_*$ plane, our proposal distribution consists of a uniform probability of jumping from current location (t_{*i}, M_{*i}) to another point (t_{*i+1}, M_{*i+1}) that is at a distance of at most r_{prop} from the current location, with r_{prop} tuned to obtain an acceptance rate of about 30%.

Similar uniform distributions are chosen for A_V and the distance to the source d . For the inclination angle, the proposal function takes the form of a unitary jump between neighboring inclination angles. We use a total number of $n_{\text{iter}} = 10^6$ iterations. It is customary to ignore a certain number of traces at the start of the MCMC trace, because early in the chain the algorithm has not yet converged. Here we set this burn-in period to 20% of the total number of elements in the trace. In order to check for convergence of the MCMC method, we use the Geweke test.

3.5. A Probabilistic Model for Unresolved Images

We consider two sources to be unresolved in the *Spitzer* bands if their UKIDSS coordinates are $2''$ apart or less. Although the resolution of the IRAC images is below this number ($\sim 1''.2$), disentangling them using simple PSF fitting might be problematic, and we therefore consider them to be unresolved for the purposes of flux estimation. Yet, because the point response functions (PRFs) for the IRAC bands are sampled every fifth of a pixel, additional information about how much each source in the cluster contributes to the unresolved fluxes is contained in the images. Here we develop

an approach to image fitting that is complementary to the model-dependent SED fitting. In Section 3.6 we describe how the two approaches complement each other.

The idea is simple: using the models for the oversampled PRFs in each IRAC band and the position of the cluster members in the resolved (UKIDSS) images as priors for the location of the sources in the unresolved (IRAC) images, we can build a probabilistic model that can be fit to reproduce the observed IRAC images. The model depends on the following parameters: the position of each source on the IRAC image (x_i, y_i) , the multiplicative scale factor A_i for each individual PRF (related to the contribution of each source to the total flux in each pixel), and the background level B .

We assume that the observed *Spitzer* images are the result of two separate processes. First, at the individual pixel level, photons hit the detector with a certain average rate that can be modeled as a Poisson process.⁵ That is, we spatially discretize the image by assuming that for each pixel, photons arrive independently of each other at a constant rate so that there is an average number of photon hits per unit time. Second, we assume that for each pixel, such a process happens as many times as we have sources in the cluster. We assume that independent Poisson processes happen simultaneously in each pixel for each source that contributes to the flux in that pixel. In other words, we assume that the image is the result of a mixture of PRFs.

Explicitly, we assume that the probability of measuring an image containing m sources with flux density N_k in the k th pixel, given the parameters of our model, that is, the set of PRF scaling factors A_i , the positions (x_i, y_i) of the sources in the IRAC images, and a uniform background level B , and assuming that the fluxes of neighboring pixels are uncorrelated, can be expressed as the product of Poisson distributions:

$$P(\{N_k\}|A) = \prod_{k=1}^{n_k} \frac{D_k^{N_k} e^{-D_k}}{N_k!}, \quad (8)$$

where D_k is the average number of photons reaching the k th pixel per unit time (i.e., the flux density in the k th pixel), and n_k is the total number of pixels in the image. Note that in this equation, each of the D_k is in fact a linear combination of the corresponding elements of the m PRFs centered at the location of the sources (from the resolved images), plus a background term:

$$D_k = n_0 \left[\sum_i^m A_i \times \text{PSF}_i + B \right]. \quad (9)$$

We fit the observed images in all four bands using this probabilistic model, and for each tested model we use the UKIDSS coordinates to choose the PRF subsample that corresponds to the location within the IRAC pixels. Since the UKIDSS source positions are known with a precision of $\sim 0''.3$, we allow for a variation of ± 1 in the actual subsampled PRF used when we perform the fitting. For the scaling factors and background and source positions, we assume uniform priors and sample the resulting posterior distribution using MCMC. The posterior probabilities for the PRF scaling factors are

⁵ We use a Poisson process here because we want the model to be applicable in low-photon-count scenarios (e.g., X-ray astronomy). In the high-photon-count regime, the Poisson model generalizes to a normal model.

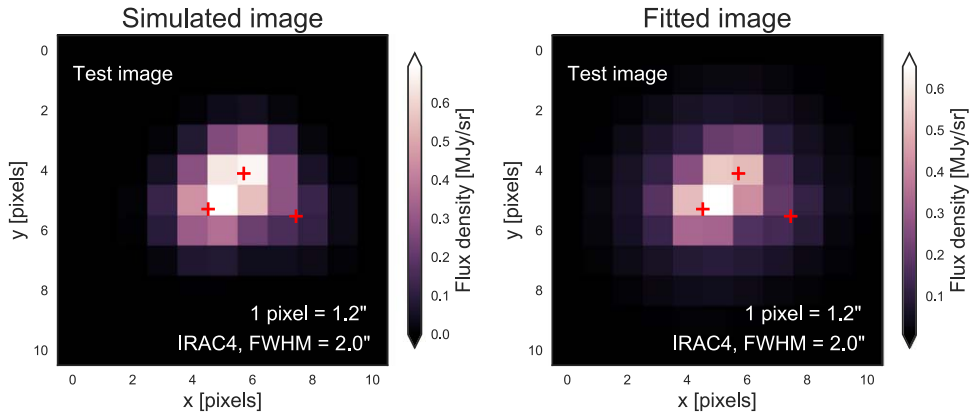


Figure 2. IRAC $8\ \mu\text{m}$ images of a simulated cluster of blended YSOs indicating the position of the individual sources with red crosses. The left panel corresponds to the originally simulated image, while the right panel shows the best fit using our method.

directly related to the flux contributed by each source to the unresolved photometry.

3.6. Assessing the Reliability of the Method

The SED and image fitting algorithms described in the previous section can be used iteratively in order to reduce the variance in the estimates of the physical parameters of the individual YSOs, by using the output flux posteriors of one method as priors in the other method. Here we describe how we combine the two in order to improve the quality of our results, and then we validate the reliability of the method by applying it to a simulated cluster with known physical parameters.

3.6.1. Iterative Fitting of the SEDs and the Images

Given the set of resolved NIR and unresolved MIR photometry for a given cluster, we perform the fitting of the data in three steps.

Step 1. Using the model of Equation (1), we simultaneously fit the SEDs of the cluster members and obtain posterior probabilities for the model parameters. We also obtain posterior predictive distributions for the unresolved fluxes in this step. The posterior predictive is the distribution of unobserved photometry \tilde{D} conditioned on the observed data D . It is constructed by averaging the likelihood of new unseen data points over all possible parameter values, weighted by their posterior probability:

$$p(\tilde{D}|D) = \int p(\tilde{D}|\Theta)p(\Theta|D)d\Theta. \quad (10)$$

Note that the probability of measuring a given unresolved flux for a given cluster member, given the observed data, equals the likelihood of that flux given the model parameters times the probability of that particular choice of parameters, marginalized over all possible parameter values. We can obtain a posterior predictive for each of the unresolved bands, for each of the cluster members. Visually, the posterior predictive can be understood as the histogram of all of the model fluxes in a particular band when the models are taken from the MCMC sampled parameters.

Step 2. Using the image -fitting model from Equations (8) and (9), we then fit the observed IRAC images and derive posterior probabilities for the fluxes in the unresolved bands. We use the posterior predictives derived in step 1 for the relative fluxes as priors for the image fitting. Note that this is consistent from a statistical point of view, since we are not

using the same information in both models. While for the SED fitting we use the *integrated* fluxes to constrain the unresolved fluxes, in the image fitting we are using the pixel-by-pixel fluxes. We get new posterior distributions for the fluxes as an output of the image fitting.

Step 3. Finally, we refit the SEDs, but this time we use the posterior probabilities for the fluxes obtained in the previous step as individual photometric measurements in the unresolved bands. We do this for all four IRAC bands, but not for the MIPS $24\ \mu\text{m}$ band, since at the MIPS resolution of $6''$ we would not get a good constraint on the unresolved fluxes since the UKIDSS sources are within $2''$ only. The end result of this three-step fitting algorithm is the best-fitting SED and images in each band, as well as the posterior probabilities for the relevant model parameters, evaluated for each individual source in the cluster.

3.6.2. Simulated Cluster

In order to assess the reliability of our method in recovering the physical parameters of clustered YSOs, we have tested it on simulated clusters composed of three YSOs whose properties have been sampled from the library of R06 models. We have simulated the coordinates of these objects from a 2D normal probability density function with a standard deviation corresponding to the typical size of the clusters in our sample ($\sim 2''$). We assigned UKIDSS, IRAC, and MIPS photometry to each source according to the corresponding R06 SEDs, and we then added 10% Gaussian noise. We also simulated IRAC images of simulated clusters by convolving the Gaussian profiles of the point sources with a model of the instrument PSF and then binning the convolved image to resemble the IRAC pixels and matching the total fluxes with the SED fluxes. In Figure 2 we show an example of a simulated IRAC 1 image compared with the result of our image-fitting algorithm. The cluster is effectively unresolved within the IRAC beam, as is the case in many real clusters for which SED fitting of the individual members is algorithmically difficult and in fact has not been attempted so far. Our approach allows for detailed modeling of the individual sources.

Following the steps described above, we first fit the set of resolved and unresolved photometry to obtain posterior probability distributions for the unresolved IRAC fluxes of the simulated cluster. The posterior predictives for the unresolved fluxes of each individual source are in excellent agreement with the ground truth values, as shown in Figure 3.

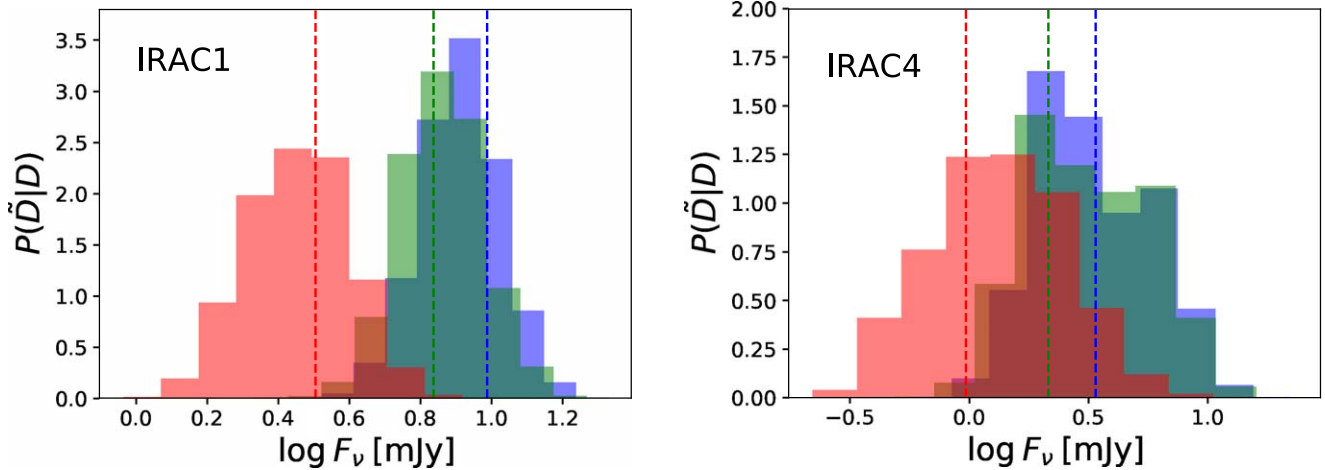


Figure 3. Posterior predictives from our deblending SED fitting approach (shaded histograms) compared with the ground truth photometry of a simulated blended cluster, for IRAC bands 1 and 4. Each histogram corresponds to the distribution of possible fluxes for one particular source, and the dashed lines represent the corresponding true value of the photometry.

We then fit the IRAC images using those posterior probabilities as priors for the relative contributions of each source, and finally we refitted the SEDs using the posterior predictives from image fitting as resolved mid-infrared data points. The final results are the posterior probability distributions for the physical parameters. In Table 1 we compare the ground truth values for the model parameters with the credible intervals resulting from our Bayesian fitting. In our experiments with simulated clusters, the ground truth values fall within or very close to the 1σ credible intervals for all individual sources. We therefore expect our parameter estimation to be reliable within the uncertainties of the R06 models themselves.

4. Results

This section summarizes the results of applying the SED/image fitting method described in the previous section to the 70 low-mass YSO clusters listed in Table 2. These results consist of the simultaneous fits to the blended SEDs, the best-fitting IRAC images generated by the image-fitting algorithm, and the derived posterior distributions for the model parameters after both methods have been combined.

4.1. SED and Image Fitting

To illustrate our SED-fitting method, in Figure 4 we show fits to the photometry of two blended clusters (IDs 6307 and 1364), each containing three protostars. The left panels show the simultaneous fits to the resolved UKIDSS photometry and the unresolved GLIMPSE photometry of each of the individual sources in each cluster. The middle panels show the resulting posterior predictives (Equation (10)) for the flux in IRAC band 1. These quantify the uncertainties in the unresolved fluxes derived from our SED-fitting method that are later used as priors for the image fitting. The right panels show fits to the SEDs of the same objects once the predicted photometry from the image-fitting algorithm is incorporated (step 3 in Section 3.6).

Next, the posterior predictives in the middle panels of Figure 4 are used as priors for the 2D fitting of the IRAC images. Figure 5 shows the resulting fits to the data for sources 6307 and 1364, in IRAC bands 1 and 4, respectively. Also shown are the updated posteriors for the flux contribution for

Table 1
Comparison with Simulated Cluster

Parameter	1σ Interval	True value
$\log t_*^1$	$5.75_{-0.10}^{0.34}$	5.88
$\log m_*^1$	$0.07_{-0.12}^{0.23}$	0.30
$\log A_V^1$	$0.84_{-1.19}^{0.16}$	1.00
$\log t_*^2$	$6.21_{-0.50}^{0.44}$	6.37
$\log m_*^2$	$0.27_{-0.29}^{0.09}$	0.37
$\log A_V^2$	$0.87_{-0.17}^{0.11}$	1.00
$\log t_*^3$	$6.18_{-0.42}^{0.46}$	6.07
$\log m_*^3$	$-0.12_{-0.24}^{0.32}$	0.01
$\log A_V^3$	$0.81_{-0.43}^{0.19}$	1.00

these two sources, after image fitting has been performed. The latter significantly reduces the variance in the estimated flux of the dominant sources, at the expense of larger variances for the dimmer sources, which do not contribute much to the total flux. Individual source flux densities are estimated by integrating over the modeled PRFs, for each source in a given cluster, and converted into millijansky. The 1σ uncertainties in these flux densities are given by the 13.6% and 86.4% percentiles of the posterior PDFs.

The right panels of Figure 4 show the resulting fits when the updated resolved photometry is included. Similar results are obtained for most individual sources within the clusters. We note that the *Herschel* mission observed both of these sources with PACS and SPIRE at 70, 160, 250, 350, and 500 μm . We have retrieved the *Herschel* photometry from Guzmán et al. (2015). For ID 1364, the retrieved fluxes fall within the 1σ region of the posterior predictives for the corresponding wavelengths. For the weaker source, ID 6307, the projected *Herschel* fluxes were below the detection limits. This agreement with measurements at longer wavelengths that were not included in the fit is an excellent sanity check for our method and highlights its predictive power.

The flux posteriors in the right panels of Figure 5 can now be reinterpreted as *resolved* photometric measurements with associated uncertainties in each band and included in the SED fitting. The estimated fluxes in the IRAC bands and their uncertainties are listed in Table 2. Our predicted individual

Table 2
GLIMPSE Sources, Derived Fluxes, and Physical Parameters

Source ID	α	δ	d (kpc)	δd (kpc)	$F_{3.6}$ (mJy)	$F_{4.5}$ (mJy)	$F_{5.8}$ (mJy)	$F_{8.0}$ (mJy)	$\log t_*$ (yr)	$\log M_*$ (M_\odot)	$\log A_V$ (mag)
360	267.2023	-28.0199	5.9	2.0	116.87 ± 3.70	332.32 ± 8.52	582.80 ± 14.93	582.80 ± 14.93	$5.04^{+0.11}_{-0.32}$	$1.20^{+0.06}_{-0.01}$	$1.76^{+0.02}_{-0.02}$
					12.43 ± 3.13	58.17 ± 8.37	201.23 ± 14.18	201.23 ± 14.18	$5.92^{+0.25}_{-0.40}$	$1.01^{+0.14}_{-0.05}$	$1.77^{+0.03}_{-0.05}$
1062	268.3317	-25.2607	3.54	1.36	19.09 ± 5.53	5.17 ± 1.14	8.05 ± 1.72	8.05 ± 1.72	$5.23^{+0.59}_{-0.63}$	$0.56^{+0.32}_{-0.26}$	$0.75^{+0.24}_{-0.43}$
					30.76 ± 4.78	33.24 ± 1.65	29.70 ± 1.93	29.70 ± 1.93	$6.31^{+0.33}_{-1.24}$	$0.62^{+0.12}_{-0.07}$	$0.74^{+0.22}_{-0.45}$
					0.01 ± 0.02	0.00 ± 0.02	0.00 ± 0.00	0.00 ± 0.00	$6.75^{+0.14}_{-0.18}$	$-0.57^{+0.19}_{-0.18}$	$0.25^{+0.28}_{-0.42}$
1277	269.4151	-24.3469	2.88	1.35	21.23 ± 1.95	11.63 ± 1.61	9.25 ± 1.76	9.25 ± 1.76	$6.30^{+0.35}_{-0.93}$	$0.66^{+0.05}_{-0.11}$	$1.08^{+0.08}_{-0.15}$
					24.83 ± 2.02	22.40 ± 1.89	22.42 ± 1.93	22.42 ± 1.93	$6.54^{+0.27}_{-0.55}$	$0.56^{+0.11}_{-0.06}$	$0.77^{+0.19}_{-0.23}$
1364	269.9419	-24.0042	3.59	0.96	24.06 ± 3.02	27.88 ± 1.84	27.14 ± 6.37	27.14 ± 6.37	$6.35^{+0.26}_{-0.44}$	$0.66^{+0.08}_{-0.05}$	$1.28^{+0.06}_{-0.08}$
					0.05 ± 0.08	0.01 ± 0.03	0.04 ± 0.06	0.04 ± 0.06	$6.11^{+0.41}_{-0.35}$	$-0.06^{+0.27}_{-0.33}$	$0.59^{+0.35}_{-0.49}$
					4.28 ± 2.44	1.74 ± 1.61	15.70 ± 6.20	15.70 ± 6.20	$5.44^{+1.10}_{-0.38}$	$0.65^{+0.10}_{-0.33}$	$1.58^{+0.08}_{-0.16}$
1369	270.2175	-24.1208	1.28	0.09	4.97 ± 1.02	3.21 ± 0.78	3.78 ± 1.16	3.78 ± 1.16	$5.66^{+0.42}_{-0.61}$	$0.02^{+0.35}_{-0.37}$	$1.25^{+0.08}_{-0.16}$
					2.77 ± 1.24	3.35 ± 0.85	4.07 ± 1.48	4.07 ± 1.48	$5.72^{+0.66}_{-0.82}$	$-0.07^{+0.44}_{-0.48}$	$0.90^{+0.21}_{-0.38}$
					0.10 ± 0.16	0.04 ± 0.10	0.02 ± 0.08	0.02 ± 0.08	$6.20^{+0.50}_{-1.08}$	$-0.56^{+0.39}_{-0.26}$	$1.01^{+0.14}_{-0.29}$
1396	270.7117	-24.299	1.3	0.1	17.50 ± 3.09	21.33 ± 1.17	12.59 ± 3.64	12.59 ± 3.64	$6.34^{+0.32}_{-0.11}$	$0.58^{+0.07}_{-0.07}$	$1.47^{+0.02}_{-0.02}$
					8.51 ± 3.52	1.03 ± 0.48	8.71 ± 8.48	8.71 ± 8.48	$6.07^{+0.38}_{-0.40}$	$0.13^{+0.22}_{-0.36}$	$0.68^{+0.21}_{-0.46}$
1437	270.2374	-23.825	4.97	0.26	22.71 ± 1.25	34.14 ± 1.41	47.96 ± 2.84	47.96 ± 2.84	$6.13^{+0.28}_{-0.12}$	$0.75^{+0.06}_{-0.10}$	$1.21^{+0.13}_{-0.74}$
					0.10 ± 0.21	0.18 ± 0.34	1.99 ± 4.40	1.99 ± 4.40	$5.41^{+0.44}_{-0.45}$	$0.17^{+0.32}_{-0.50}$	$1.08^{+0.13}_{-0.26}$
1493	270.0784	-23.4725	2.4		0.13 ± 0.11	0.08 ± 0.11	0.11 ± 0.21	0.11 ± 0.21	$6.08^{+0.40}_{-0.41}$	$-0.03^{+0.34}_{-0.43}$	$1.23^{+0.13}_{-0.16}$
					1.47 ± 0.52	2.89 ± 0.58	5.43 ± 1.08	5.43 ± 1.08	$6.33^{+0.36}_{-0.57}$	$0.52^{+0.12}_{-0.15}$	$1.60^{+0.07}_{-0.08}$
					0.09 ± 0.11	0.06 ± 0.14	0.15 ± 0.30	0.15 ± 0.30	$5.96^{+0.38}_{-0.55}$	$-0.23^{+0.49}_{-0.34}$	$1.23^{+0.13}_{-0.17}$
1566	270.5074	-23.0983	3.81	0.77	49.15 ± 3.04	66.30 ± 4.01	67.15 ± 5.25	67.15 ± 5.25	$6.54^{+0.14}_{-0.29}$	$0.78^{+0.04}_{-0.07}$	$1.43^{+0.05}_{-0.05}$
					9.03 ± 2.95	13.54 ± 4.22	23.22 ± 5.22	23.22 ± 5.22	$6.43^{+0.19}_{-0.21}$	$0.69^{+0.06}_{-0.08}$	$1.52^{+0.04}_{-0.10}$
					0.52 ± 0.38	0.92 ± 0.82	5.03 ± 2.05	5.03 ± 2.05	$5.33^{+0.45}_{-0.36}$	$0.33^{+0.24}_{-0.56}$	$1.38^{+0.13}_{-0.14}$
1629	270.7366	-22.8421	2.7	0.5	25.14 ± 1.43	38.91 ± 1.49	59.06 ± 2.04	59.06 ± 2.04	$6.49^{+0.21}_{-0.18}$	$0.74^{+0.08}_{-0.07}$	$1.53^{+0.06}_{-0.07}$
					0.02 ± 0.01	0.01 ± 0.01	0.01 ± 0.01	0.01 ± 0.01	$6.45^{+0.33}_{-0.42}$	$-0.57^{+0.25}_{-0.21}$	$0.65^{+0.30}_{-0.30}$
					0.17 ± 0.11	0.05 ± 0.08	0.10 ± 0.27	0.10 ± 0.27	$6.10^{+0.32}_{-0.39}$	$0.44^{+0.33}_{-0.27}$	$1.51^{+0.11}_{-0.15}$
					0.10 ± 0.10	0.10 ± 0.11	0.04 ± 0.06	0.04 ± 0.06	$5.99^{+0.38}_{-0.57}$	$-0.47^{+0.44}_{-0.32}$	$0.92^{+0.14}_{-0.27}$
					2.61 ± 0.64	3.84 ± 0.62	4.78 ± 1.04	4.78 ± 1.04	$5.45^{+0.34}_{-0.16}$	$0.15^{+0.33}_{-0.13}$	$1.17^{+0.16}_{-0.30}$
1807	270.5608	-21.5428	3.47	0.75	6.91 ± 1.24	0.12 ± 0.17	0.13 ± 0.21	0.13 ± 0.21	$5.03^{+0.33}_{-0.26}$	$0.64^{+0.19}_{-0.49}$	$1.47^{+0.11}_{-0.20}$
					2.67 ± 1.05	34.76 ± 1.38	72.74 ± 2.15	72.74 ± 2.15	$6.04^{+0.27}_{-0.54}$	$0.91^{+0.02}_{-0.06}$	$1.85^{+0.02}_{-0.07}$
					0.01 ± 0.01	0.00 ± 0.00	0.00 ± 0.00	0.00 ± 0.00	$6.52^{+0.21}_{-0.46}$	$-0.51^{+0.27}_{-0.29}$	$0.81^{+0.09}_{-0.28}$
					2.69 ± 0.85	1.14 ± 0.38	1.85 ± 0.66	1.85 ± 0.66	$6.14^{+0.47}_{-0.76}$	$0.56^{+0.13}_{-0.09}$	$1.58^{+0.10}_{-0.05}$
2073	272.3163	-21.053	3.81	0.59	1.65 ± 0.55	1.68 ± 0.54	1.61 ± 0.70	1.61 ± 0.70	$6.30^{+0.09}_{-0.41}$	$0.47^{+0.02}_{-0.12}$	$1.45^{+0.02}_{-0.10}$
					12.36 ± 1.04	12.84 ± 0.91	12.29 ± 1.09	12.29 ± 1.09	$6.28^{+0.20}_{-0.21}$	$0.77^{+0.04}_{-0.09}$	$1.34^{+0.00}_{-0.04}$
2090	272.5295	-20.9922	4.13	0.51	0.39 ± 0.29	0.03 ± 0.04	0.57 ± 0.42	0.57 ± 0.42	$6.35^{+0.10}_{-0.49}$	$0.35^{+0.10}_{-0.11}$	$1.24^{+0.10}_{-0.03}$
					0.05 ± 0.06	0.03 ± 0.04	0.02 ± 0.03	0.02 ± 0.03	$6.09^{+0.49}_{-0.51}$	$0.06^{+0.23}_{-0.54}$	$0.54^{+0.28}_{-0.38}$
2130	272.5325	-20.7702	3.73	0.59	0.00 ± 0.00	0.00 ± 0.00	0.00 ± 0.00	0.00 ± 0.00	$6.57^{+0.25}_{-1.34}$	$-0.51^{+0.28}_{-0.26}$	$0.75^{+0.20}_{-0.26}$
					0.02 ± 0.05	0.00 ± 0.01	0.02 ± 0.08	0.02 ± 0.08	$5.79^{+0.64}_{-0.98}$	$-0.12^{+0.52}_{-0.32}$	$1.29^{+0.16}_{-0.18}$
					3.89 ± 0.98	8.31 ± 2.40	10.40 ± 3.10	10.40 ± 3.10	$5.75^{+0.72}_{-0.53}$	$0.64^{+0.13}_{-0.15}$	$1.52^{+0.10}_{-0.07}$
					1.25 ± 1.11	8.60 ± 2.12	11.92 ± 2.96	11.92 ± 2.96	$6.16^{+0.37}_{-0.52}$	$0.70^{+0.15}_{-0.08}$	$1.69^{+0.09}_{-0.07}$
					0.02 ± 0.02	0.01 ± 0.01	0.00 ± 0.00	0.00 ± 0.00	$6.08^{+0.44}_{-0.77}$	$-0.10^{+0.23}_{-0.49}$	$1.03^{+0.08}_{-0.27}$
					6.06 ± 2.51	4.87 ± 1.04	16.42 ± 2.14	16.42 ± 2.14	$5.06^{+0.78}_{-0.65}$	$0.53^{+0.17}_{-0.21}$	$0.57^{+0.27}_{-0.33}$
					1.11 ± 1.25	0.44 ± 0.40	1.02 ± 1.06	1.02 ± 1.06	$5.14^{+1.69}_{-0.46}$	$0.46^{+0.13}_{-0.57}$	$1.21^{+0.07}_{-0.14}$

Table 2
(Continued)

Source ID	α	δ	d (kpc)	δd (kpc)	$F_{3.6}$ (mJy)	$F_{4.5}$ (mJy)	$F_{5.8}$ (mJy)	$F_{8.0}$ (mJy)	$\log t_*$ (yr)	$\log M_*$ (M_\odot)	$\log A_V$ (mag)
2133	271.9143	-20.4448	2.73	0.84	8.19 ± 2.33	7.81 ± 1.83	7.63 ± 2.48	7.63 ± 2.48	$5.36^{+0.87}_{-0.31}$	$0.50^{+0.14}_{-0.11}$	$1.34^{+0.07}_{-0.14}$
					8.05 ± 2.48	10.88 ± 2.01	16.72 ± 3.22	16.72 ± 3.22	$6.38^{+0.29}_{-0.35}$	$0.64^{+0.08}_{-0.08}$	$1.57^{+0.05}_{-0.09}$
2141	271.9798	-20.4531	2.63	0.87	19.98 ± 1.84	26.22 ± 3.38	33.12 ± 2.85	33.12 ± 2.85	$6.36^{+0.26}_{-0.33}$	$0.67^{+0.09}_{-0.05}$	$1.55^{+0.05}_{-0.05}$
					1.94 ± 1.52	1.68 ± 1.88	3.12 ± 2.33	3.12 ± 2.33	$5.31^{+0.67}_{-0.28}$	$0.49^{+0.16}_{-0.34}$	$1.49^{+0.07}_{-0.10}$
2412	272.6466	-19.2146	3.59	0.56	20.03 ± 1.66	19.40 ± 1.37	17.45 ± 2.50	17.45 ± 2.50	$6.50^{+0.26}_{-0.22}$	$0.64^{+0.12}_{-0.08}$	$1.28^{+0.07}_{-0.08}$
					1.61 ± 1.04	2.75 ± 1.22	3.57 ± 2.48	3.57 ± 2.48	$5.71^{+0.96}_{-0.44}$	$0.29^{+0.22}_{-0.42}$	$1.11^{+0.11}_{-0.18}$
					0.15 ± 0.13	0.08 ± 0.07	0.02 ± 0.03	0.02 ± 0.03	$6.14^{+0.33}_{-0.40}$	$-0.08^{+0.26}_{-0.31}$	$0.29^{+0.31}_{-0.62}$
2416	273.0237	-19.3811	3.80	0.52	0.29 ± 0.28	0.26 ± 0.34	0.14 ± 0.23	0.14 ± 0.23	$5.75^{+0.47}_{-0.44}$	$-0.04^{+0.37}_{-0.37}$	$1.05^{+0.15}_{-0.35}$
					0.00 ± 0.00	0.00 ± 0.00	0.00 ± 0.00	0.00 ± 0.00	$5.39^{+0.07}_{-0.22}$	$-0.67^{+0.11}_{-0.11}$	$0.12^{+0.10}_{-0.24}$
					0.09 ± 0.06	0.00 ± 0.00	0.03 ± 0.01	0.03 ± 0.01	$6.28^{+0.13}_{-0.13}$	$0.18^{+0.10}_{-0.09}$	$1.14^{+0.15}_{-0.05}$
2419	272.6617	-19.188	3.59	0.56	0.01 ± 0.01	0.00 ± 0.00	0.01 ± 0.01	0.01 ± 0.01	$5.54^{+0.36}_{-0.04}$	$-0.76^{+0.03}_{-0.24}$	$-0.45^{+0.06}_{-0.26}$
					0.01 ± 0.01	3.62 ± 3.77	6.82 ± 4.17	6.82 ± 4.17	$4.48^{+0.08}_{-0.07}$	$-0.22^{+0.15}_{-0.23}$	$0.24^{+0.03}_{-0.24}$
					63.49 ± 1.95	95.97 ± 3.10	128.19 ± 3.81	128.19 ± 3.81	$6.21^{+0.07}_{-0.09}$	$0.80^{+0.04}_{-0.03}$	$1.43^{+0.04}_{-0.04}$
					7.05 ± 2.02	2.83 ± 1.51	6.73 ± 3.60	6.73 ± 3.60	$6.51^{+0.16}_{-0.15}$	$0.70^{+0.07}_{-0.15}$	$1.46^{+0.07}_{-0.05}$
					5.04 ± 2.04	21.93 ± 2.29	43.57 ± 4.27	43.57 ± 4.27	$5.20^{+0.33}_{-0.15}$	$0.61^{+0.07}_{-0.12}$	$1.09^{+0.19}_{-0.15}$
2713	273.0283	-17.6483	13.80	0.77	0.19 ± 0.15	0.19 ± 0.16	0.25 ± 0.23	0.25 ± 0.23	$6.26^{+0.51}_{-0.39}$	$0.00^{+0.20}_{-0.28}$	$0.73^{+0.44}_{-0.11}$
					0.01 ± 0.00	0.00 ± 0.00	0.00 ± 0.00	0.00 ± 0.00	$6.70^{+0.12}_{-0.11}$	$-0.65^{+0.20}_{-0.19}$	$0.00^{+0.29}_{-0.39}$
					0.02 ± 0.07	0.00 ± 0.00	0.00 ± 0.00	0.00 ± 0.00	$5.64^{+0.61}_{-0.53}$	$0.13^{+0.34}_{-0.44}$	$1.08^{+0.20}_{-0.20}$
2985	274.06	-16.9622	2.15	0.73	24.19 ± 1.89	2.06 ± 1.98	30.38 ± 2.35	30.38 ± 2.35	$6.32^{+0.21}_{-0.17}$	$0.89^{+0.08}_{-0.05}$	$0.85^{+0.16}_{-0.51}$
					4.09 ± 1.61	19.74 ± 21.43	3.28 ± 2.07	3.28 ± 2.07	$6.06^{+0.51}_{-1.07}$	$0.74^{+0.07}_{-0.08}$	$0.57^{+0.23}_{-0.36}$
					0.01 ± 0.01	0.00 ± 0.01	0.01 ± 0.01	0.01 ± 0.01	$6.54^{+0.23}_{-0.96}$	$-0.41^{+0.34}_{-0.29}$	$1.20^{+0.13}_{-0.16}$
3156	274.2054	-16.4183	3.88	0.43	0.00 ± 0.00	0.00 ± 0.00	0.00 ± 0.00	0.00 ± 0.00	$6.65^{+0.22}_{-0.38}$	$-0.72^{+0.27}_{-0.20}$	$0.69^{+0.21}_{-0.38}$
					0.58 ± 0.60	0.42 ± 0.45	1.54 ± 1.41	1.54 ± 1.41	$5.84^{+0.47}_{-0.30}$	$0.02^{+0.33}_{-0.36}$	$1.36^{+0.09}_{-0.09}$
					7.84 ± 1.03	8.17 ± 0.79	8.53 ± 1.37	8.53 ± 1.37	$6.28^{+0.39}_{-0.49}$	$0.52^{+0.06}_{-0.07}$	$1.29^{+0.05}_{-0.06}$
3227	274.8098	-16.5083	2.09	0.71	0.00 ± 0.00	0.00 ± 0.00	0.00 ± 0.00	0.00 ± 0.00	$5.94^{+0.64}_{-0.91}$	$-0.37^{+0.44}_{-0.33}$	$1.17^{+0.21}_{-0.39}$
					1.43 ± 0.61	3.18 ± 0.73	3.65 ± 1.16	3.65 ± 1.16	$5.22^{+1.03}_{-0.89}$	$0.58^{+0.22}_{-0.40}$	$1.36^{+0.24}_{-0.52}$
					4.07 ± 0.82	1.32 ± 0.51	1.21 ± 0.66	1.21 ± 0.66	$5.70^{+0.85}_{-0.54}$	$0.46^{+0.10}_{-0.40}$	$0.94^{+0.18}_{-0.24}$
3282	274.4012	-16.0383	2.72	0.61	7.44 ± 1.06	12.37 ± 1.08	14.61 ± 1.55	14.61 ± 1.55	$6.29^{+0.32}_{-0.52}$	$0.71^{+0.17}_{-0.10}$	$1.56^{+0.07}_{-0.09}$
					6.21 ± 1.33	6.73 ± 1.20	9.71 ± 2.05	9.71 ± 2.05	$5.69^{+0.90}_{-0.82}$	$0.57^{+0.14}_{-0.18}$	$1.58^{+0.05}_{-0.09}$
3538	275.2079	-14.7652	4.07	0.38	1.85 ± 1.00	2.50 ± 1.11	3.44 ± 1.80	3.44 ± 1.80	$5.60^{+0.65}_{-0.49}$	$0.34^{+0.20}_{-0.39}$	$1.43^{+0.08}_{-0.10}$
					0.00 ± 0.00	0.00 ± 0.00	0.00 ± 0.00	0.00 ± 0.00	$6.52^{+0.30}_{-0.25}$	$-0.48^{+0.29}_{-0.32}$	$1.08^{+0.12}_{-0.12}$
					20.91 ± 1.80	24.15 ± 2.14	28.73 ± 3.11	28.73 ± 3.11	$6.17^{+0.37}_{-1.37}$	$0.72^{+0.15}_{-0.08}$	$1.50^{+0.05}_{-0.04}$
3568	275.7657	-14.9323	3.74	0.42	0.07 ± 0.07	0.04 ± 0.05	0.05 ± 0.10	0.05 ± 0.10	$6.36^{+0.31}_{-0.30}$	$-0.53^{+0.28}_{-0.25}$	$0.27^{+0.39}_{-0.53}$
					2.98 ± 1.45	6.73 ± 1.86	6.53 ± 2.68	6.53 ± 2.68	$5.36^{+0.62}_{-0.43}$	$0.57^{+0.18}_{-0.42}$	$1.45^{+0.10}_{-0.15}$
					13.08 ± 3.25	8.87 ± 4.12	8.21 ± 5.67	8.21 ± 5.67	$6.45^{+0.15}_{-0.17}$	$0.70^{+0.10}_{-0.08}$	$1.48^{+0.05}_{-0.04}$
3749	274.7755	-13.598	1.8	0.1	0.01 ± 0.01	0.05 ± 0.04	0.07 ± 0.11	0.07 ± 0.11	$5.85^{+0.74}_{-0.22}$	$-0.24^{+0.29}_{-0.29}$	$1.28^{+0.02}_{-0.14}$
					11.25 ± 3.72	29.01 ± 3.33	38.00 ± 5.11	38.00 ± 5.11	$6.32^{+0.08}_{-0.16}$	$0.94^{+0.15}_{-0.17}$	$1.62^{+0.09}_{-0.11}$
					1.40 ± 2.11	0.62 ± 0.94	1.28 ± 1.94	1.28 ± 1.94	$6.56^{+0.16}_{-0.66}$	$0.47^{+0.20}_{-0.34}$	$1.48^{+0.05}_{-0.14}$
3749	274.7755	-13.598	1.8	0.1	0.00 ± 0.00	0.00 ± 0.00	0.00 ± 0.00	0.00 ± 0.00	$6.61^{+0.26}_{-0.24}$	$-0.29^{+0.07}_{-0.28}$	$0.57^{+0.13}_{-0.23}$
					0.00 ± 0.00	0.00 ± 0.00	0.00 ± 0.00	0.00 ± 0.00	$6.46^{+0.06}_{-0.48}$	$-0.75^{+0.35}_{-0.13}$	$0.77^{+0.18}_{-0.29}$
					2.18 ± 0.85	3.33 ± 0.98	17.19 ± 6.20	17.19 ± 6.20	$6.50^{+0.23}_{-0.27}$	$0.66^{+0.14}_{-0.14}$	$1.69^{+0.05}_{-0.09}$
3749	274.7755	-13.598	1.8	0.1	3.97 ± 1.03	9.40 ± 1.20	9.44 ± 3.19	9.44 ± 3.19	$3.70^{+0.49}_{-0.38}$	$1.35^{+0.05}_{-0.09}$	$1.32^{+0.11}_{-0.14}$
					1.68 ± 1.44	1.37 ± 1.07	2.17 ± 1.52	2.17 ± 1.52	$5.59^{+0.44}_{-0.66}$	$-0.13^{+0.49}_{-0.30}$	$1.29^{+0.08}_{-0.14}$

Table 2
(Continued)

Source ID	α	δ	d (kpc)	δd (kpc)	$F_{3.6}$ (mJy)	$F_{4.5}$ (mJy)	$F_{5.8}$ (mJy)	$F_{8.0}$ (mJy)	$\log t_*$ (yr)	$\log M_*$ (M_\odot)	$\log A_V$ (mag)
3756	274.6668	−13.51	1.8	0.1	19.21 ± 1.73	18.01 ± 1.48	16.01 ± 1.85	16.01 ± 1.85	6.57 ^{+0.24} _{−0.05}	0.52 ^{+0.07} _{−0.05}	1.38 ^{+0.04} _{−0.05}
					7.57 ± 1.23	10.29 ± 1.53	12.99 ± 2.42	12.99 ± 2.42	6.47 ^{+0.31} _{−0.27}	0.57 ^{+0.13} _{−0.07}	1.66 ^{+0.05} _{−0.04}
3776	275.2404	−13.7086	1.99	0.64	1.82 ± 1.48	5.82 ± 1.72	8.27 ± 2.60	8.27 ± 2.60	5.84 ^{+0.63} _{−0.33}	0.33 ^{+0.17} _{−0.37}	1.55 ^{+0.05} _{−0.07}
					5.75 ± 1.39	7.43 ± 1.58	8.50 ± 2.21	8.50 ± 2.21	5.86 ^{+0.66} _{−0.34}	0.34 ^{+0.13} _{−0.43}	0.90 ^{+0.12} _{−0.19}
3786	274.8371	−13.4591	1.8	0.1	3.92 ± 1.54	5.96 ± 1.69	3.75 ± 2.35	3.75 ± 2.35	5.90 ^{+0.51} _{−0.34}	0.18 ^{+0.21} _{−0.47}	0.85 ^{+0.16} _{−0.29}
					9.58 ± 1.10	8.31 ± 0.90	9.03 ± 1.37	9.03 ± 1.37	5.30 ^{+0.37} _{−0.45}	0.12 ^{+0.36} _{−0.24}	1.05 ^{+0.19} _{−0.36}
4013	276.3031	−12.741	11.84	0.40	1.88 ± 0.82	1.42 ± 0.77	2.35 ± 1.40	2.35 ± 1.40	5.67 ^{+0.61} _{−0.60}	−0.04 ^{+0.38} _{−0.34}	1.16 ^{+0.12} _{−0.23}
					14.25 ± 1.57	6.07 ± 1.30	9.95 ± 1.70	9.95 ± 1.70	6.36 ^{+0.26} _{−0.21}	0.86 ^{+0.08} _{−0.13}	1.12 ^{+0.05} _{−0.08}
4101	276.713	−12.4251	4.71	0.31	0.02 ± 0.02	0.05 ± 0.12	0.02 ± 0.05	0.02 ± 0.05	6.19 ^{+0.31} _{−1.38}	0.49 ^{+0.28} _{−0.55}	1.31 ^{+0.13} _{−0.24}
					39.26 ± 1.95	40.06 ± 1.77	40.69 ± 2.08	40.69 ± 2.08	6.31 ^{+0.16} _{−0.15}	1.00 ^{+0.15} _{−0.09}	1.24 ^{+0.05} _{−0.11}
4101	276.713	−12.4251	4.71	0.31	17.11 ± 3.07	24.36 ± 5.02	21.13 ± 4.14	21.13 ± 4.14	5.69 ^{+0.81} _{−0.95}	0.71 ^{+0.29} _{−0.11}	1.03 ^{+0.12} _{−0.33}
					8.14 ± 4.62	9.37 ± 8.35	6.81 ± 5.46	6.81 ± 5.46	5.73 ^{+0.86} _{−0.97}	0.62 ^{+0.23} _{−0.15}	1.19 ^{+0.09} _{−0.19}
4745	278.6758	−8.5279	6.05	0.36	7.06 ± 1.21	8.06 ± 1.37	8.93 ± 2.45	8.93 ± 2.45	5.43 ^{+0.89} _{−0.87}	0.93 ^{+0.22} _{−0.12}	1.42 ^{+0.10} _{−0.11}
					3.03 ± 1.13	4.81 ± 1.27	6.12 ± 2.26	6.12 ± 2.26	5.65 ^{+0.56} _{−0.73}	0.96 ^{+0.15} _{−0.10}	1.56 ^{+0.10} _{−0.12}
4750	278.6704	−8.5073	6.05	0.36	0.01 ± 0.02	0.00 ± 0.00	0.20 ± 0.20	0.20 ± 0.20	4.80 ^{+0.40} _{−0.68}	0.63 ^{+0.19} _{−0.18}	0.95 ^{+0.30} _{−0.30}
					3.34 ± 1.49	3.65 ± 1.74	8.05 ± 1.99	8.05 ± 1.99	6.02 ^{+0.34} _{−0.19}	0.82 ^{+0.12} _{−0.08}	1.73 ^{+0.05} _{−0.08}
4796	278.6437	−8.1738	<1.27		3.07 ± 1.25	4.45 ± 3.79	3.93 ± 2.14	3.93 ± 2.14	6.48 ^{+0.24} _{−1.11}	0.57 ^{+0.14} _{−0.13}	1.27 ^{+0.05} _{−0.11}
					0.42 ± 0.50	0.58 ± 0.87	0.90 ± 1.15	0.90 ± 1.15	6.06 ^{+0.28} _{−0.64}	0.84 ^{+0.09} _{−0.13}	1.68 ^{+0.14} _{−0.07}
4796	278.6437	−8.1738	<1.27		0.75 ± 0.54	0.62 ± 0.57	1.38 ± 0.91	1.38 ± 0.91	4.86 ^{+0.21} _{−0.18}	−0.84 ^{+0.08} _{−0.10}	0.58 ^{+0.14} _{−0.15}
					5.92 ± 1.73	3.31 ± 1.73	0.67 ± 1.54	0.67 ± 1.54	5.95 ^{+0.00} _{−0.13}	−0.64 ^{+0.25} _{−0.02}	1.19 ^{+0.01} _{−0.03}
4816	278.5914	−8.0471	3.10	0.44	2.15 ± 2.43	1.59 ± 1.48	0.80 ± 0.74	0.80 ± 0.74	6.95 ^{+0.05} _{−0.16}	−0.98 ^{+0.22} _{−0.01}	1.10 ^{+0.10} _{−0.16}
					15.60 ± 1.78	27.84 ± 2.78	42.27 ± 2.09	42.27 ± 2.09	6.22 ^{+0.12} _{−0.00}	0.74 ^{+0.02} _{−0.07}	1.57 ^{+0.00} _{−0.03}
4816	278.5914	−8.0471	3.10	0.44	1.13 ± 0.84	0.87 ± 0.64	1.02 ± 0.72	1.02 ± 0.72	5.51 ^{+0.35} _{−0.33}	0.12 ^{+0.38} _{−0.40}	1.31 ^{+0.11} _{−0.14}
					8.95 ± 1.69	2.47 ± 1.44	0.41 ± 0.58	0.41 ± 0.58	5.12 ^{+0.54} _{−0.33}	0.42 ^{+0.39} _{−0.35}	0.79 ^{+0.18} _{−0.17}
4955	278.5693	−7.2357	6.38	0.48	0.01 ± 0.00	0.02 ± 0.01	0.27 ± 0.21	0.27 ± 0.21	6.77 ^{+0.13} _{−0.25}	−0.75 ^{+0.15} _{−0.16}	0.82 ^{+0.18} _{−0.12}
					6.12 ± 1.34	9.90 ± 1.47	14.83 ± 1.69	14.83 ± 1.69	5.13 ^{+1.30} _{−0.85}	0.76 ^{+0.26} _{−0.13}	1.49 ^{+0.10} _{−0.18}
4955	278.5693	−7.2357	6.38	0.48	1.55 ± 0.78	2.46 ± 0.86	0.24 ± 0.52	0.24 ± 0.52	5.18 ^{+0.59} _{−0.31}	0.20 ^{+0.35} _{−0.26}	1.38 ^{+0.08} _{−0.12}
					7.04 ± 2.30	11.97 ± 2.27	16.42 ± 4.43	16.42 ± 4.43	6.73 ^{+0.00} _{−0.06}	0.65 ^{+0.00} _{−0.11}	−1.40 ^{+0.00} _{−0.00}
5201	279.6925	−6.4813	5.93	0.42	0.14 ± 0.12	0.01 ± 0.00	0.00 ± 0.01	0.00 ± 0.01	6.63 ^{+0.00} _{−0.00}	−0.15 ^{+0.08} _{−0.00}	1.03 ^{+0.02} _{−0.00}
					1.27 ± 0.64	0.32 ± 0.35	3.91 ± 4.59	3.91 ± 4.59	3.67 ^{+0.00} _{−0.05}	−0.11 ^{+0.06} _{−0.00}	0.14 ^{+0.00} _{−0.00}
5201	279.6925	−6.4813	5.93	0.42	33.09 ± 3.01	43.68 ± 2.71	56.12 ± 3.68	56.12 ± 3.68	6.23 ^{+0.00} _{−0.00}	0.96 ^{+0.04} _{−0.00}	1.50 ^{+0.00} _{−0.00}
					20.85 ± 4.01	10.51 ± 3.71	12.77 ± 7.44	12.77 ± 7.44	6.32 ^{+0.00} _{−0.03}	0.77 ^{+0.00} _{−0.00}	1.48 ^{+0.00} _{−0.00}
5201	279.6925	−6.4813	5.93	0.42	9.58 ± 0.99	12.46 ± 0.93	14.59 ± 1.42	14.59 ± 1.42	4.98 ^{+0.03} _{−0.07}	0.76 ^{+0.04} _{−0.05}	1.41 ^{+0.04} _{−0.03}
					0.05 ± 0.07	0.08 ± 0.14	0.83 ± 0.61	0.83 ± 0.61	5.04 ^{+0.15} _{−0.18}	−0.30 ^{+0.48} _{−0.16}	1.29 ^{+0.10} _{−0.11}
5504	280.9674	−4.6098	3.09	0.43	0.02 ± 0.02	0.01 ± 0.03	0.01 ± 0.01	0.01 ± 0.01	6.09 ^{+0.41} _{−0.20}	−0.18 ^{+0.26} _{−0.09}	1.02 ^{+0.96} _{−0.20}
					0.70 ± 0.29	1.08 ± 0.31	1.79 ± 0.65	1.79 ± 0.65	6.32 ^{+0.00} _{−0.03}	0.77 ^{+0.00} _{−0.00}	1.48 ^{+0.00} _{−0.00}
5504	280.9674	−4.6098	3.09	0.43	0.00 ± 0.00	0.00 ± 0.00	0.00 ± 0.00	0.00 ± 0.00	6.78 ^{+0.04} _{−0.27}	0.42 ^{+0.14} _{−0.03}	0.48 ^{+0.08} _{−0.50}
					0.01 ± 0.01	0.01 ± 0.01	0.01 ± 0.01	0.01 ± 0.01	4.74 ^{+0.00} _{−0.01}	−0.55 ^{+0.12} _{−0.05}	−0.39 ^{+0.44} _{−0.00}
5559	281.0159	−4.2557	4.64	0.39	6.24 ± 1.51	10.33 ± 2.29	10.98 ± 1.93	10.98 ± 1.93	5.55 ^{+0.85} _{−0.00}	−0.47 ^{+0.00} _{−0.20}	1.33 ^{+0.12} _{−0.00}
					20.71 ± 1.93	21.69 ± 2.11	26.02 ± 2.36	26.02 ± 2.36	5.78 ^{+0.00} _{−0.62}	0.58 ^{+0.09} _{−0.37}	1.51 ^{+0.00} _{−0.13}
5559	281.0159	−4.2557	4.64	0.39	0.01 ± 0.01	0.00 ± 0.02	0.00 ± 0.01	0.00 ± 0.01	5.65 ^{+0.11} _{−0.68}	0.62 ^{+0.03} _{−0.34}	1.50 ^{+0.03} _{−0.11}
					0.34 ± 0.37	0.24 ± 0.37	0.21 ± 0.40	0.21 ± 0.40	6.00 ^{+0.55} _{−0.98}	−0.27 ^{+0.46} _{−0.37}	0.98 ^{+0.17} _{−0.30}
					7.57 ± 1.02	8.20 ± 0.81	10.52 ± 1.23	10.52 ± 1.23	5.64 ^{+0.62} _{−0.56}	0.34 ^{+0.25} _{−0.40}	0.66 ^{+0.27} _{−0.45}

Table 2
(Continued)

Source ID	α	δ	d (kpc)	δd (kpc)	$F_{3.6}$ (mJy)	$F_{4.5}$ (mJy)	$F_{5.8}$ (mJy)	$F_{8.0}$ (mJy)	$\log t_*$ (yr)	$\log M_*$ (M_\odot)	$\log A_V$ (mag)
5686	280.9778	-3.4684	4.62	0.40	7.95 ± 1.40	17.46 ± 2.27	17.34 ± 3.66	17.34 ± 3.66	$6.09^{+0.56}_{-1.02}$	$0.57^{+0.15}_{-0.11}$	$0.60^{+0.26}_{-0.44}$
					0.00 ± 0.00	0.00 ± 0.00	0.00 ± 0.00	0.00 ± 0.00	$6.53^{+0.12}_{-0.28}$	$0.78^{+0.15}_{-0.13}$	$1.60^{+0.05}_{-0.10}$
					16.52 ± 1.79	16.37 ± 2.37	29.28 ± 3.78	29.28 ± 3.78	$6.48^{+0.22}_{-0.43}$	$-0.17^{+0.21}_{-0.38}$	$0.91^{+0.16}_{-0.13}$
					0.01 ± 0.02	0.00 ± 0.00	0.00 ± 0.00	0.00 ± 0.00	$6.23^{+0.16}_{-0.07}$	$0.77^{+0.20}_{-0.17}$	$1.78^{+0.08}_{-0.07}$
					0.00 ± 0.00	0.00 ± 0.00	0.00 ± 0.00	0.00 ± 0.00	$6.60^{+0.19}_{-0.32}$	$-0.13^{+0.19}_{-0.30}$	$0.26^{+0.32}_{-0.60}$
5976	281.904	-2.1462	7.08	0.50	0.42 ± 0.58	0.23 ± 0.32	0.90 ± 1.15	0.90 ± 1.15	$6.48^{+0.19}_{-0.18}$	$-0.48^{+0.16}_{-0.33}$	$0.28^{+0.40}_{-0.30}$
					23.42 ± 3.07	31.14 ± 3.41	35.26 ± 5.47	35.26 ± 5.47	$4.39^{+0.28}_{-0.90}$	$-0.02^{+1.40}_{-0.29}$	$1.35^{+0.80}_{-0.39}$
					19.45 ± 2.55	26.97 ± 2.74	35.48 ± 4.61	35.48 ± 4.61	$5.40^{+0.33}_{-0.77}$	$0.92^{+0.55}_{-0.06}$	$1.44^{+0.16}_{-0.12}$
					2.23 ± 1.45	2.56 ± 1.64	8.13 ± 2.30	8.13 ± 2.30	$4.56^{+0.15}_{-0.24}$	$1.31^{+0.15}_{-0.25}$	$1.42^{+0.10}_{-0.16}$
					2.03 ± 1.23	3.10 ± 1.49	5.21 ± 1.38	5.21 ± 1.38	$5.02^{+1.36}_{-0.62}$	$0.95^{+0.29}_{-0.31}$	$1.41^{+0.23}_{-0.30}$
5997	282.0054	-2.0609	7.33	0.25	9.77 ± 1.02	16.49 ± 1.15	28.63 ± 1.91	28.63 ± 1.91	$5.89^{+0.29}_{-0.33}$	$0.76^{+0.15}_{-0.08}$	$1.44^{+0.14}_{-0.07}$
					0.28 ± 0.48	0.40 ± 0.76	0.68 ± 0.92	0.68 ± 0.92	$6.28^{+0.21}_{-0.10}$	$0.79^{+0.08}_{-0.05}$	$1.45^{+0.08}_{-0.15}$
					4.45 ± 1.69	4.01 ± 1.48	2.91 ± 1.03	2.91 ± 1.03	$5.74^{+1.42}_{-0.69}$	$0.48^{+0.09}_{-0.60}$	$1.30^{+0.11}_{-0.25}$
6004	282.0535	-2.0414	7.07	0.50	19.32 ± 2.26	17.49 ± 1.98	17.39 ± 3.14	17.39 ± 3.14	$5.28^{+0.26}_{-0.39}$	$0.74^{+0.32}_{-0.17}$	$0.98^{+0.18}_{-0.21}$
					0.06 ± 0.07	0.17 ± 0.17	0.16 ± 0.16	0.16 ± 0.16	$6.12^{+0.20}_{-0.19}$	$0.75^{+0.06}_{-0.08}$	$0.76^{+0.11}_{-0.19}$
					39.90 ± 2.21	32.65 ± 1.81	32.19 ± 2.74	32.19 ± 2.74	$5.38^{+1.22}_{-0.56}$	$0.29^{+0.28}_{-0.35}$	$1.03^{+0.20}_{-0.51}$
					0.01 ± 0.01	0.00 ± 0.00	0.00 ± 0.00	0.00 ± 0.00	$6.20^{+0.23}_{-0.34}$	$0.89^{+0.08}_{-0.08}$	$1.42^{+0.04}_{-0.05}$
					3.10 ± 0.86	5.58 ± 0.99	4.92 ± 1.33	4.92 ± 1.33	$6.41^{+0.17}_{-0.22}$	$-0.29^{+0.15}_{-0.34}$	$0.33^{+0.19}_{-0.60}$
6028	281.718	-1.7779	7.07	0.95	4.43 ± 0.95	6.90 ± 0.98	6.59 ± 1.46	6.59 ± 1.46	$6.31^{+0.20}_{-0.22}$	$0.73^{+0.17}_{-0.13}$	$1.58^{+0.09}_{-0.10}$
					0.01 ± 0.02	0.00 ± 0.00	0.00 ± 0.00	0.00 ± 0.00	$6.40^{+0.22}_{-0.15}$	$0.81^{+0.15}_{-0.16}$	$1.62^{+0.06}_{-0.07}$
					8.77 ± 2.20	7.03 ± 1.50	7.45 ± 2.35	7.45 ± 2.35	$6.17^{+0.55}_{-0.25}$	$-0.06^{+0.27}_{-0.24}$	$0.51^{+0.40}_{-0.18}$
					0.04 ± 0.05	0.03 ± 0.05	0.01 ± 0.03	0.01 ± 0.03	$6.35^{+0.28}_{-0.22}$	$0.72^{+0.12}_{-0.08}$	$1.28^{+0.08}_{-0.08}$
					0.23 ± 0.26	0.18 ± 0.24	0.10 ± 0.18	0.10 ± 0.18	$5.99^{+0.42}_{-0.73}$	$0.18^{+0.21}_{-0.41}$	$1.20^{+0.14}_{-0.17}$
6148	282.1367	-1.1541	7.01	1.02	7.35 ± 2.59	4.71 ± 1.38	4.95 ± 1.75	4.95 ± 1.75	$6.03^{+0.47}_{-0.38}$	$0.40^{+0.12}_{-0.19}$	$0.25^{+0.36}_{-0.44}$
					0.56 ± 0.29	0.65 ± 0.46	1.58 ± 1.10	1.58 ± 1.10	$6.46^{+0.30}_{-0.43}$	$0.60^{+0.12}_{-0.09}$	$0.79^{+0.22}_{-0.35}$
					0.01 ± 0.02	0.00 ± 0.01	0.01 ± 0.02	0.01 ± 0.02	$5.29^{+0.74}_{-0.77}$	$-0.22^{+0.65}_{-0.19}$	$0.89^{+0.22}_{-0.43}$
					0.91 ± 0.34	2.82 ± 0.66	4.42 ± 1.32	4.42 ± 1.32	$6.05^{+0.72}_{-0.50}$	$-0.55^{+0.38}_{-0.18}$	$0.85^{+0.14}_{-0.41}$
6256	282.466	-0.4041	3.14	0.45	0.00 ± 0.00	0.00 ± 0.00	0.00 ± 0.00	0.00 ± 0.00	$6.63^{+0.15}_{-0.54}$	$0.54^{+0.11}_{-0.13}$	$1.55^{+0.06}_{-0.05}$
					2.15 ± 0.74	3.17 ± 0.69	6.28 ± 1.22	6.28 ± 1.22	$5.49^{+0.22}_{-0.38}$	$-0.54^{+0.43}_{-0.21}$	$0.22^{+0.34}_{-0.35}$
					0.01 ± 0.01	0.00 ± 0.00	0.00 ± 0.01	0.00 ± 0.01	$6.42^{+0.19}_{-0.24}$	$0.66^{+0.16}_{-0.07}$	$0.45^{+0.27}_{-0.74}$
					3.41 ± 4.18	1.21 ± 2.05	17.61 ± 16.33	17.61 ± 16.33	$5.96^{+0.70}_{-0.64}$	$0.21^{+0.17}_{-0.43}$	$0.64^{+0.36}_{-0.36}$
					2.50 ± 5.54	8.22 ± 25.34	12.25 ± 36.49	12.25 ± 36.49	$6.22^{+0.28}_{-0.20}$	$0.75^{+0.18}_{-0.10}$	$1.40^{+0.11}_{-0.13}$
6286	282.8543	-0.2419	11.35	0.46	7.22 ± 1.34	9.09 ± 1.38	8.72 ± 1.78	8.72 ± 1.78	$6.32^{+0.36}_{-0.16}$	$0.68^{+0.12}_{-0.11}$	$1.17^{+0.12}_{-0.13}$
					0.45 ± 0.30	0.36 ± 0.26	0.45 ± 0.54	0.45 ± 0.54	$5.84^{+0.46}_{-0.63}$	$-0.04^{+0.33}_{-0.46}$	$1.56^{+0.06}_{-0.09}$
					2.85 ± 1.23	2.60 ± 1.09	4.27 ± 2.00	4.27 ± 2.00	$6.37^{+0.34}_{-0.59}$	$-0.63^{+0.35}_{-0.21}$	$1.32^{+0.06}_{-0.07}$
					11.46 ± 2.22	9.67 ± 1.24	18.98 ± 4.53	18.98 ± 4.53	$6.25^{+0.36}_{-0.64}$	$-0.46^{+0.43}_{-0.27}$	$1.20^{+0.12}_{-0.09}$
6307	282.4882	0.0925	0.56	0.54	0.05 ± 0.06	0.02 ± 0.03	0.01 ± 0.01	0.01 ± 0.01	$5.82^{+0.20}_{-1.06}$	$0.74^{+0.20}_{-0.15}$	$1.55^{+0.09}_{-0.10}$
					2.30 ± 8.13	13.22 ± 1.27	12.58 ± 17.48	12.58 ± 17.48	$5.75^{+0.67}_{-0.87}$	$-0.10^{+0.60}_{-0.42}$	$0.80^{+0.27}_{-0.38}$
					0.00 ± 0.00	0.58 ± 0.43	0.82 ± 0.59	0.82 ± 0.59	$6.08^{+0.32}_{-0.37}$	$0.84^{+0.14}_{-0.11}$	$1.76^{+0.08}_{-0.09}$
					0.13 ± 0.19	0.21 ± 0.32	0.42 ± 0.67	0.42 ± 0.67	$5.75^{+0.69}_{-0.59}$	$0.42^{+0.36}_{-0.62}$	$1.60^{+0.16}_{-0.14}$
					0.00 ± 0.00	0.00 ± 0.00	0.00 ± 0.00	0.00 ± 0.00	$5.81^{+0.60}_{-0.59}$	$-0.36^{+1.10}_{-0.38}$	$1.84^{+0.38}_{-0.48}$
6512	283.3616	1.264	3.58	0.46	1.32 ± 0.76	0.71 ± 0.36	7.50 ± 3.66	7.50 ± 3.66	$4.72^{+0.04}_{-0.32}$	$0.01^{+0.35}_{-0.31}$	$0.02^{+0.60}_{-0.61}$
					9.03 ± 1.00	13.32 ± 0.84	9.19 ± 2.97	9.19 ± 2.97	$5.18^{+0.34}_{-0.38}$	$0.22^{+0.22}_{-0.24}$	$1.41^{+0.08}_{-0.28}$

Table 2
(Continued)

Source ID	α	δ	d (kpc)	δd (kpc)	$F_{3.6}$ (mJy)	$F_{4.5}$ (mJy)	$F_{5.8}$ (mJy)	$F_{8.0}$ (mJy)	$\log t_*$ (yr)	$\log M_*$ (M_\odot)	$\log A_V$ (mag)
6572	284.2129	1.3027	2.96	0.47	0.00 ± 0.01	0.02 ± 0.02	0.02 ± 0.03	0.02 ± 0.03	$6.36^{+0.21}_{-0.20}$	$0.62^{+0.14}_{-0.09}$	$1.37^{+0.08}_{-0.07}$
					2.54 ± 0.80	1.86 ± 0.70	3.82 ± 1.52	3.82 ± 1.52	$5.54^{+1.16}_{-1.89}$	$-0.42^{+0.46}_{-0.36}$	$0.94^{+0.20}_{-0.75}$
					4.12 ± 0.88	6.45 ± 0.89	6.68 ± 1.58	6.68 ± 1.58	$5.92^{+0.34}_{-0.30}$	$0.44^{+0.12}_{-0.34}$	$1.20^{+0.08}_{-0.13}$
6590	283.3846	1.7837	3.61	0.47	0.00 ± 0.01	0.01 ± 0.01	0.00 ± 0.01	0.00 ± 0.01	$6.56^{+0.14}_{-0.36}$	$0.56^{+0.09}_{-0.06}$	$1.44^{+0.05}_{-0.04}$
					2.77 ± 0.62	7.61 ± 0.96	16.58 ± 1.78	16.58 ± 1.78	$6.54^{+0.26}_{-0.32}$	$-0.03^{+0.14}_{-0.20}$	$1.44^{+0.14}_{-0.12}$
					3.30 ± 0.74	4.59 ± 0.93	8.03 ± 2.07	8.03 ± 2.07	$5.16^{+0.00}_{-0.00}$	$0.75^{+0.00}_{-0.00}$	$1.63^{+0.03}_{-0.01}$
6747	284.1658	2.3252	3.72	0.48	2.10 ± 1.03	0.99 ± 0.64	0.88 ± 0.70	0.88 ± 0.70	$6.36^{+0.26}_{-0.18}$	$0.57^{+0.10}_{-0.00}$	$1.55^{+0.00}_{-0.06}$
					17.85 ± 1.42	15.93 ± 1.10	20.28 ± 1.58	20.28 ± 1.58	$5.64^{+0.45}_{-0.36}$	$0.30^{+0.25}_{-0.35}$	$0.68^{+0.22}_{-0.33}$
					0.08 ± 0.11	0.04 ± 0.07	0.04 ± 0.08	0.04 ± 0.08	$6.39^{+0.26}_{-0.25}$	$0.65^{+0.07}_{-0.05}$	$1.39^{+0.04}_{-0.04}$
7137	285.2823	5.1651	1.88	0.46	12.87 ± 2.08	9.70 ± 1.36	6.47 ± 1.89	6.47 ± 1.89	$6.04^{+0.33}_{-0.87}$	$-0.25^{+0.43}_{-0.31}$	$0.73^{+0.25}_{-0.77}$
					22.53 ± 1.95	26.09 ± 1.60	32.33 ± 2.08	32.33 ± 2.08	$5.48^{+0.62}_{-0.37}$	$0.42^{+0.15}_{-0.35}$	$1.32^{+0.06}_{-0.09}$
					7.37 ± 1.84	7.73 ± 1.81	9.67 ± 2.35	9.67 ± 2.35	$6.55^{+0.20}_{-0.36}$	$0.54^{+0.07}_{-0.07}$	$1.37^{+0.04}_{-0.04}$
7143	285.2769	5.1949	1.88	0.46	6.90 ± 2.13	6.92 ± 1.76	7.62 ± 2.56	7.62 ± 2.56	$5.58^{+0.93}_{-0.54}$	$0.49^{+0.12}_{-0.30}$	$1.45^{+0.05}_{-0.10}$
					2.40 ± 0.56	5.75 ± 0.94	9.75 ± 1.39	9.75 ± 1.39	$5.54^{+0.51}_{-0.40}$	$0.32^{+0.24}_{-0.34}$	$1.51^{+0.07}_{-0.10}$
					0.15 ± 0.25	0.12 ± 0.33	0.21 ± 0.99	0.21 ± 0.99	$6.05^{+0.58}_{-1.29}$	$0.64^{+0.17}_{-0.15}$	$1.68^{+0.07}_{-0.16}$
7276	286.1944	6.0907	8.39	0.64	5.46 ± 1.31	6.71 ± 0.99	7.79 ± 1.53	7.79 ± 1.53	$5.79^{+0.56}_{-0.71}$	$0.02^{+0.39}_{-0.47}$	$1.32^{+0.13}_{-0.16}$
					3.43 ± 1.53	1.95 ± 0.84	2.90 ± 1.43	2.90 ± 1.43	$6.06^{+0.47}_{-1.20}$	$0.75^{+0.21}_{-0.09}$	$1.28^{+0.07}_{-0.14}$
					1.12 ± 0.85	1.08 ± 1.70	3.19 ± 3.08	3.19 ± 3.08	$5.65^{+0.91}_{-0.66}$	$0.62^{+0.12}_{-0.15}$	$0.56^{+0.26}_{-0.42}$
7492	287.454	8.0791	5.19	0.90	25.11 ± 1.45	29.55 ± 3.01	37.64 ± 2.34	37.64 ± 2.34	$6.37^{+0.72}_{-0.32}$	$0.57^{+0.11}_{-0.18}$	$1.27^{+0.13}_{-0.21}$
					3.36 ± 0.71	8.53 ± 1.10	13.46 ± 1.59	13.46 ± 1.59	$6.28^{+0.26}_{-0.13}$	$0.80^{+0.04}_{-0.05}$	$1.46^{+0.03}_{-0.04}$
					0.64 ± 0.50	1.83 ± 0.91	2.14 ± 1.28	2.14 ± 1.28	$5.73^{+0.47}_{-0.81}$	$0.95^{+0.25}_{-0.09}$	$1.70^{+0.07}_{-0.14}$
7516	287.5937	8.9819	11.20	0.50	2.93 ± 1.01	6.34 ± 1.88	8.21 ± 2.25	8.21 ± 2.25	$5.51^{+0.79}_{-0.87}$	$0.83^{+0.29}_{-0.19}$	$1.58^{+0.14}_{-0.15}$
					2.39 ± 1.22	3.46 ± 1.87	4.87 ± 2.47	4.87 ± 2.47	$5.95^{+0.56}_{-0.94}$	$0.71^{+0.08}_{-0.11}$	$1.46^{+0.08}_{-0.13}$
					1.25 ± 0.93	1.09 ± 1.06	2.28 ± 2.53	2.28 ± 2.53	$5.47^{+0.95}_{-0.63}$	$0.66^{+0.10}_{-0.21}$	$1.40^{+0.11}_{-0.18}$
7569	287.9451	9.7828	5.93	1.44	12.03 ± 1.30	28.54 ± 1.78	45.91 ± 2.74	45.91 ± 2.74	$5.70^{+0.88}_{-0.51}$	$0.60^{+0.09}_{-0.14}$	$1.37^{+0.07}_{-0.11}$
					5.16 ± 1.27	9.93 ± 1.41	13.60 ± 1.93	13.60 ± 1.93	$3.62^{+0.33}_{-0.20}$	$0.33^{+0.49}_{-0.05}$	$1.08^{+0.11}_{-0.14}$
					3.16 ± 1.23	5.58 ± 1.73	6.48 ± 1.84	6.48 ± 1.84	$6.23^{+0.40}_{-1.45}$	$0.62^{+0.33}_{-0.23}$	$1.13^{+0.13}_{-0.30}$
7580	287.9335	9.9845	5.91	2.10	2.50 ± 0.85	3.59 ± 1.00	8.74 ± 1.85	8.74 ± 1.85	$5.26^{+0.96}_{-0.56}$	$0.54^{+0.16}_{-0.24}$	$1.23^{+0.12}_{-0.10}$
					10.20 ± 1.06	16.89 ± 1.19	24.67 ± 1.95	24.67 ± 1.95	$6.36^{+0.21}_{-0.84}$	$0.69^{+0.12}_{-0.07}$	$1.44^{+0.07}_{-0.13}$
					0.02 ± 0.05	0.00 ± 0.01	0.05 ± 0.13	0.05 ± 0.13	$6.23^{+0.21}_{-0.08}$	$0.93^{+0.11}_{-0.08}$	$1.62^{+0.06}_{-0.11}$
7590	287.9285	10.1183	4.76	1.14	0.00 ± 0.00	0.00 ± 0.00	0.00 ± 0.00	0.00 ± 0.00	$5.78^{+0.40}_{-0.37}$	$0.19^{+0.20}_{-0.34}$	$0.48^{+0.31}_{-0.59}$
					12.67 ± 1.03	10.86 ± 0.87	9.77 ± 1.57	9.77 ± 1.57	$6.29^{+0.31}_{-0.23}$	$-0.07^{+0.20}_{-0.27}$	$0.33^{+0.27}_{-0.50}$
					0.73 ± 0.52	0.20 ± 0.33	0.78 ± 1.23	0.78 ± 1.23	$5.40^{+1.12}_{-0.63}$	$0.44^{+0.15}_{-0.34}$	$1.11^{+0.17}_{-0.29}$
8304	292.2463	17.8265	9.76	0.56	1.74 ± 0.64	4.20 ± 1.65	5.43 ± 2.00	5.43 ± 2.00	$5.79^{+0.54}_{-0.73}$	$-0.10^{+0.41}_{-0.39}$	$1.07^{+0.13}_{-0.25}$
					3.81 ± 0.76	8.09 ± 1.22	11.45 ± 1.66	11.45 ± 1.66	$6.10^{+0.52}_{-0.82}$	$0.48^{+0.14}_{-0.10}$	$1.67^{+0.08}_{-0.10}$
					8.62 ± 0.96	6.52 ± 0.74	8.31 ± 1.00	8.31 ± 1.00	$6.44^{+0.29}_{-0.42}$	$0.59^{+0.10}_{-0.08}$	$1.71^{+0.04}_{-0.07}$
8376	292.5529	18.3298	1.92	0.64	0.61 ± 0.55	0.25 ± 0.42	0.12 ± 0.24	0.12 ± 0.24	$6.00^{+0.60}_{-0.41}$	$0.49^{+0.06}_{-0.15}$	$1.08^{+0.08}_{-0.13}$
					3.22 ± 1.34	5.61 ± 1.26	7.97 ± 2.37	7.97 ± 2.37	$5.99^{+0.43}_{-0.49}$	$-0.23^{+0.40}_{-0.30}$	$0.81^{+0.19}_{-0.36}$
					0.02 ± 0.02	0.02 ± 0.02	0.01 ± 0.01	0.01 ± 0.01	$5.82^{+0.64}_{-1.18}$	$0.81^{+0.27}_{-0.16}$	$1.65^{+0.11}_{-0.15}$
8745	294.8893	23.9764	2.16	0.10	2.04 ± 1.46	3.81 ± 1.54	6.33 ± 2.51	6.33 ± 2.51	$6.07^{+0.44}_{-0.81}$	$-0.10^{+0.32}_{-0.43}$	$0.40^{+0.34}_{-0.45}$
					6.77 ± 1.94	7.63 ± 1.49	7.41 ± 2.11	7.41 ± 2.11	$5.75^{+0.70}_{-1.01}$	$0.75^{+0.25}_{-0.19}$	$1.63^{+0.12}_{-0.18}$
					2.36 ± 1.47	2.04 ± 1.23	2.34 ± 1.55	2.34 ± 1.55	$5.31^{+1.21}_{-0.59}$	$0.64^{+0.21}_{-0.16}$	$0.95^{+0.38}_{-0.38}$
8870	296.7318	25.2053	2.5		0.79 ± 0.62	0.90 ± 0.79	0.96 ± 0.90	0.96 ± 0.90	$5.67^{+0.81}_{-0.79}$	$0.59^{+0.34}_{-0.22}$	$0.91^{+0.18}_{-0.35}$
					0.61 ± 0.55	0.25 ± 0.42	0.12 ± 0.24	0.12 ± 0.24			
					3.22 ± 1.34	5.61 ± 1.26	7.97 ± 2.37	7.97 ± 2.37			
18398	265.9022	-30.5484	<5.22		0.02 ± 0.02	0.02 ± 0.02	0.01 ± 0.01	0.01 ± 0.01			
					2.04 ± 1.46	3.81 ± 1.54	6.33 ± 2.51	6.33 ± 2.51			
					6.77 ± 1.94	7.63 ± 1.49	7.41 ± 2.11	7.41 ± 2.11			
18695	265.7287	-29.3484	<6.01		2.36 ± 1.47	2.04 ± 1.23	2.34 ± 1.55	2.34 ± 1.55			
					0.79 ± 0.62	0.90 ± 0.79	0.96 ± 0.90	0.96 ± 0.90			

Table 2
(Continued)

Source ID	α	δ	d (kpc)	δd (kpc)	$F_{3.6}$ (mJy)	$F_{4.5}$ (mJy)	$F_{5.8}$ (mJy)	$F_{8.0}$ (mJy)	$\log t_*$ (yr)	$\log M_*$ (M_\odot)	$\log A_V$ (mag)
18738	266.1215	-29.402	<7.00		3.70 ± 1.09	1.77 ± 0.95	6.85 ± 1.86	6.85 ± 1.86	$5.47^{+0.91}_{-0.85}$	$0.60^{+0.27}_{-0.30}$	$1.40^{+0.12}_{-0.16}$
					4.10 ± 1.42	16.53 ± 1.32	21.10 ± 2.11	21.10 ± 2.11	$6.36^{+0.25}_{-0.25}$	$0.75^{+0.12}_{-0.09}$	$1.64^{+0.08}_{-0.06}$
					$6.27^{+0.22}_{-0.15}$	$0.89^{+0.11}_{-0.07}$	$1.71^{+0.06}_{-0.05}$				

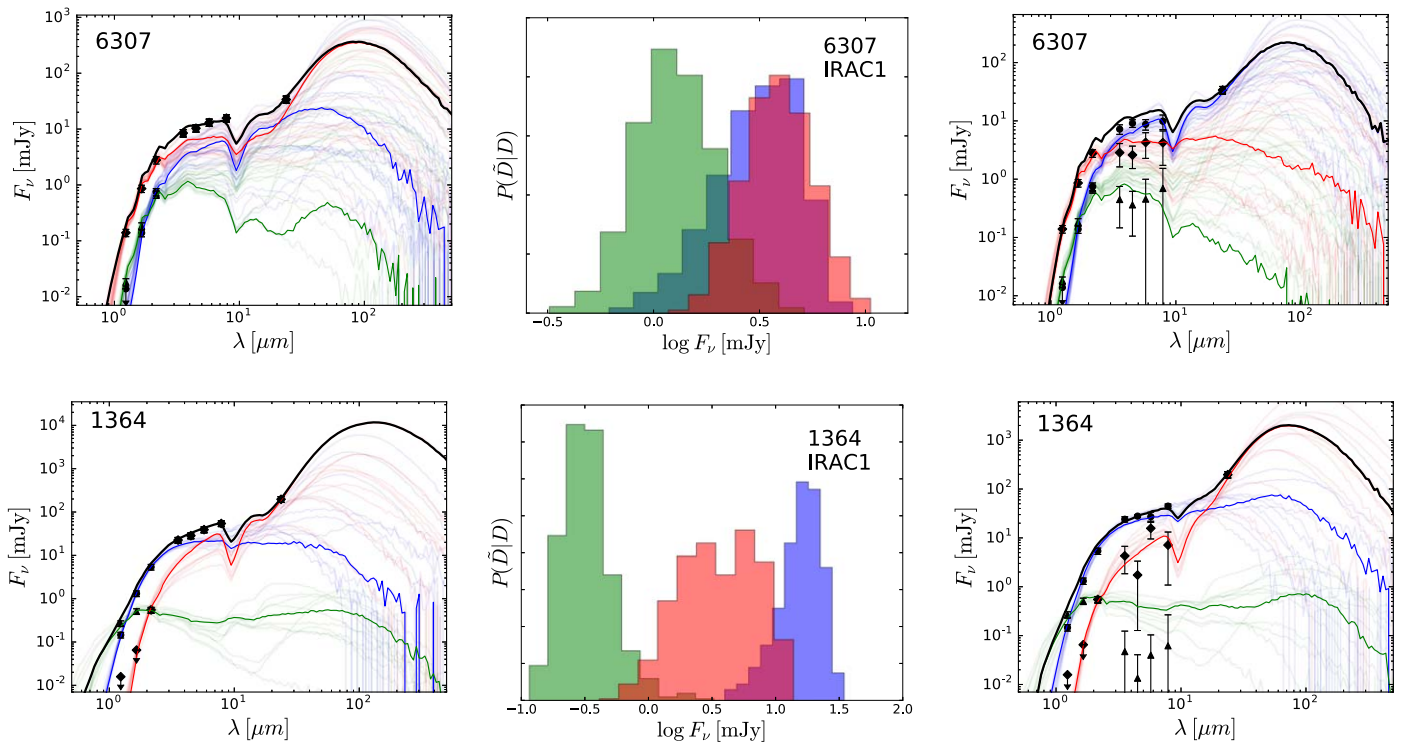


Figure 4. Simultaneous SED fitting of spatially blended sources in clusters 6307 (upper panels) and 1364 (lower panels). The left panels show the initial SED fit when only unresolved information is available from the IRAC bands. Each source is shown in a different color and with different symbols for the measured photometry. The solid lines correspond to the MAP estimate, whereas the shaded lines correspond to the solutions within 1σ of the best fit. The middle panels show the posterior predictive for the IRAC 1 band fluxes derived from fitting the unresolved SEDs. The right panels show the resolved fit after constraints from the image-fitting algorithm have been incorporated. The IRAC fluxes resulting from sampling the image-fitting posteriors now appear as resolved measurements with associated error bars.

luminosities will soon be put to the test using *James Webb Space Telescope* (*JWST*) observations. With a spatial resolution six or seven times larger than *Spitzer*-IRAC, *JWST*-MIRI will be able to resolve most of our clusters into individual YSOs, using filters centered at similar wavelengths, such as F560W and F770W.

An example of the final model parameter posteriors can be seen in Figure 6 for cluster 6307. Plotted are the posteriors for stellar mass (m_*), age (t_*), and visual extinction (A_V) for each of the three individual sources. For each YSO in the cluster, mass and age are degenerate, and the marginalized probabilities typically show two possible solutions, with one of the two probability maxima being significantly more prominent. It would be extremely hard to spot these two solutions for individual unresolved YSOs using conventional SED-fitting methods. The estimated visual extinctions are well constrained and typically have scatters of 0.3–0.4 dex and mean values below 40 mag.

For 6307, our results indicate similar evolutionary stages for all three YSOs composing the cluster. The MAP estimates for the individual ages are all within a 0.6 Myr range centered around 6 Myr. More generally, age uncertainties are still significant (of the order of ± 0.5 Myr or more), and coeval birth of the three protostars cannot be assumed based on this evidence alone. We discuss the likelihood of coeval birth within individual clusters in Section 5.3.

For YSOs in a given cluster, the NIR fluxes from UKIDSS do not necessarily correlate with YSO mass. A significant fraction of the stellar luminosity is reprocessed and reemitted at MIR wavelengths. Correctly associating NIR sources with MIR fluxes is crucial to estimating the intrinsic luminosities of each

member, their masses, and the amount of obscuration due to dust absorption in each case. Our method can do exactly that. For example, cluster 1364 contains a dim, embedded NIR source (red SED in the lower panels of Figure 4) that nevertheless dominates the IRAC and MIPS bands and that is significantly more massive than what would be expected from its UKIDSS fluxes only. Given the spatial projected proximity of this source to one other member of the cluster, it would have been very difficult to estimate its mass using conventional techniques.

4.2. Derived Properties of Clustered YSOs

We now describe the derived properties for the YSOs in our sample and look at the correlations found between those properties. We focus on three main aspects: (1) overall statistics; (2) cluster-to-cluster variations in mass, age, and extinction; and (3) variations of YSO properties within individual clusters.

4.2.1. Overall Statistics

Figure 7 shows histograms of the YSO masses, ages, and visual extinctions of all 207 individual sources that make up the 70 studied clusters. The values plotted correspond to the 50th percentile from the MCMC sample chains. On average, there are three detected sources per cluster, and clusters with two detected members are significantly more common (28 out of 70 clusters) than multiple clusters. The measured mass distribution is bimodal with a main peak at $m_* \sim 3.0 M_\odot$ and a secondary peak at $m_* \sim 0.8 M_\odot$. The maximum derived mass is $m_* \sim 22 M_\odot$.

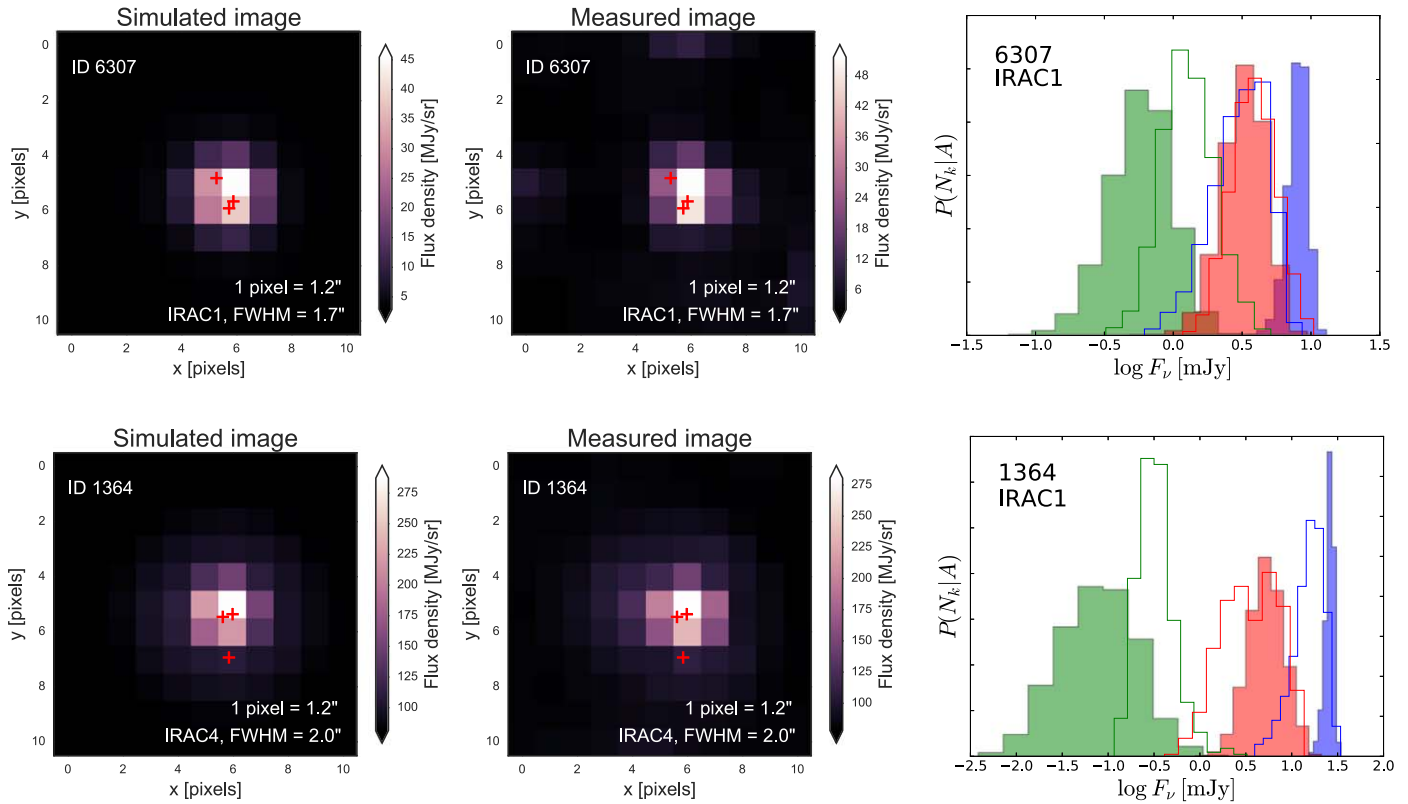


Figure 5. Left panels: MAP estimates from 2D image fitting for sources 6307 and 1364 in IRAC bands 1 and 4, respectively. Middle panels: original measured images for the same sources in the corresponding bands, for source ID 6307 in IRAC bands 1 and 4. The red crosses indicate the locations of the UKIDSS sources. Right panels: posterior distributions ($P(\{N_k\}|A)$) for the fluxes after image fitting. The color coding is the same as in Figure 4. For comparison, the posteriors after the original SED fitting are shown as the solid-line histograms.

The age distribution is consistent with a relatively evolved population; that is, most sources have derived ages compatible with them being class II or class III YSOs, with only 11 out of the 207 YSOs being 10^5 years or younger. This is not surprising given the fact that we have selected sources with clear NIR detections. The distribution peaks at 2.5 Myr and is more skewed toward younger ages.

The large majority of clusters are located in regions of high visual extinction relative to the average A_V for individual stars at the same distances, as derived from the Pan-STARRS data. For example, at distances of 15 kpc or less, Green et al. (2015) derive $E(B - V)$ values in the galactic plane that are consistent with $A_V < 10$ mag, whereas our distribution of A_V values peaks at about 20 mag. Such increased extinction toward the YSO clusters is expected and confirms that clustered star formation occurs in regions that are significantly more embedded than neighboring field stars; the broad distribution of A_V for these young stars is perhaps of more interest. The fact that extinctions higher than about $A_V = 50$ are not detected is probably a selection effect, since those sources are harder to detect in the NIR.

4.2.2. Cluster-to-cluster Properties

Figure 8 shows the projected location of our YSO clusters onto the galactic plane, color coded respectively by the derived MAP values of (a) $\log M_{cl}$, the total stellar mass in the cluster estimated as the sum of the individual masses detected; (b) $\log m_{max}$, the mass of the most massive member in the cluster; (c) $\log t_*$, the estimated age of the cluster; and (d) $\log A_V$,

the estimated visual extinction. The range of cluster stellar masses in our clusters (uncorrected for incompleteness) is $1.5 M_\odot < M_{cl} < 45 M_\odot$, and it contains between two and five detected members. On the other hand, the range of most massive stars in each cluster is $0.9 M_\odot < m_{max} < 22 M_\odot$, which suggests that the mass of detected mass in these clusters is dominated by the most massive star, with significant contributions from the second most massive in some cases. About 90% of the studied clusters are closer to us than half the distance to the most distant cluster in the sample. The most massive YSO detected (located in cluster 3568), with a mass of $22 M_\odot$, is at a distance of 3.7 kpc, just beyond the Sagittarius arm at a galactic longitude of (l) $\sim 16^\circ$. This is relatively close compared with the most distant cluster, located at almost 15 kpc from us. This same source is also one of the least evolved Class I sources. Its $24 \mu\text{m}$ flux density is almost an order of magnitude higher than that of other cluster members. The fact that the most massive source detected as part of a cluster is not particularly far away hints at the fact that selection effects of distance on measured masses, at least within the distance range considered here, are not dramatic. However, in Section 4.3, we take distance effects into account when we correct M_{cl} for the effects of completeness.

As for the spatial distribution of evolutionary stages, cluster 5976 has the youngest age, estimated as the mean of the individual YSO ages. It has five members and is only 3 arcsec apart from a maser source identified in Szymczak et al. (2005), in the far end of the 3 kpc arm, a clear indication of massive star formation taking place in the region. The most evolved cluster is 5686, which also contains five members and is

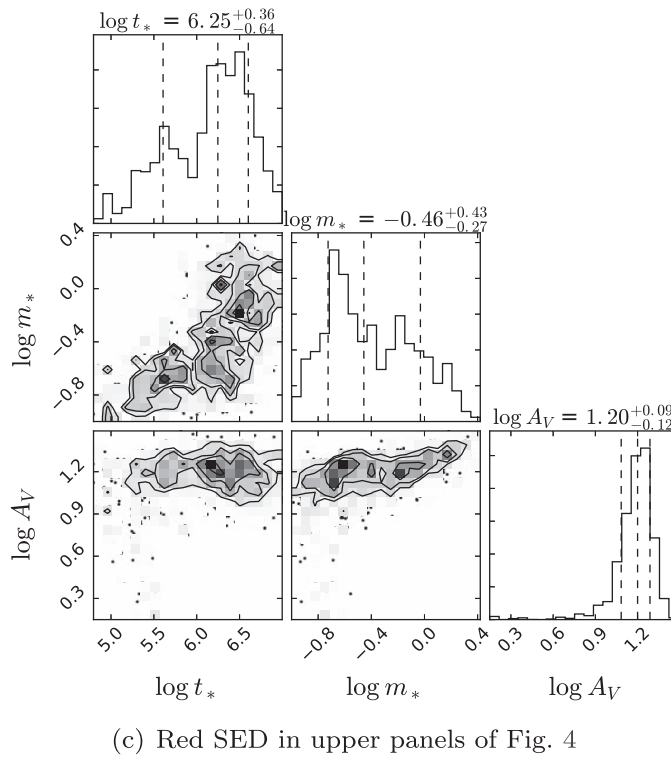
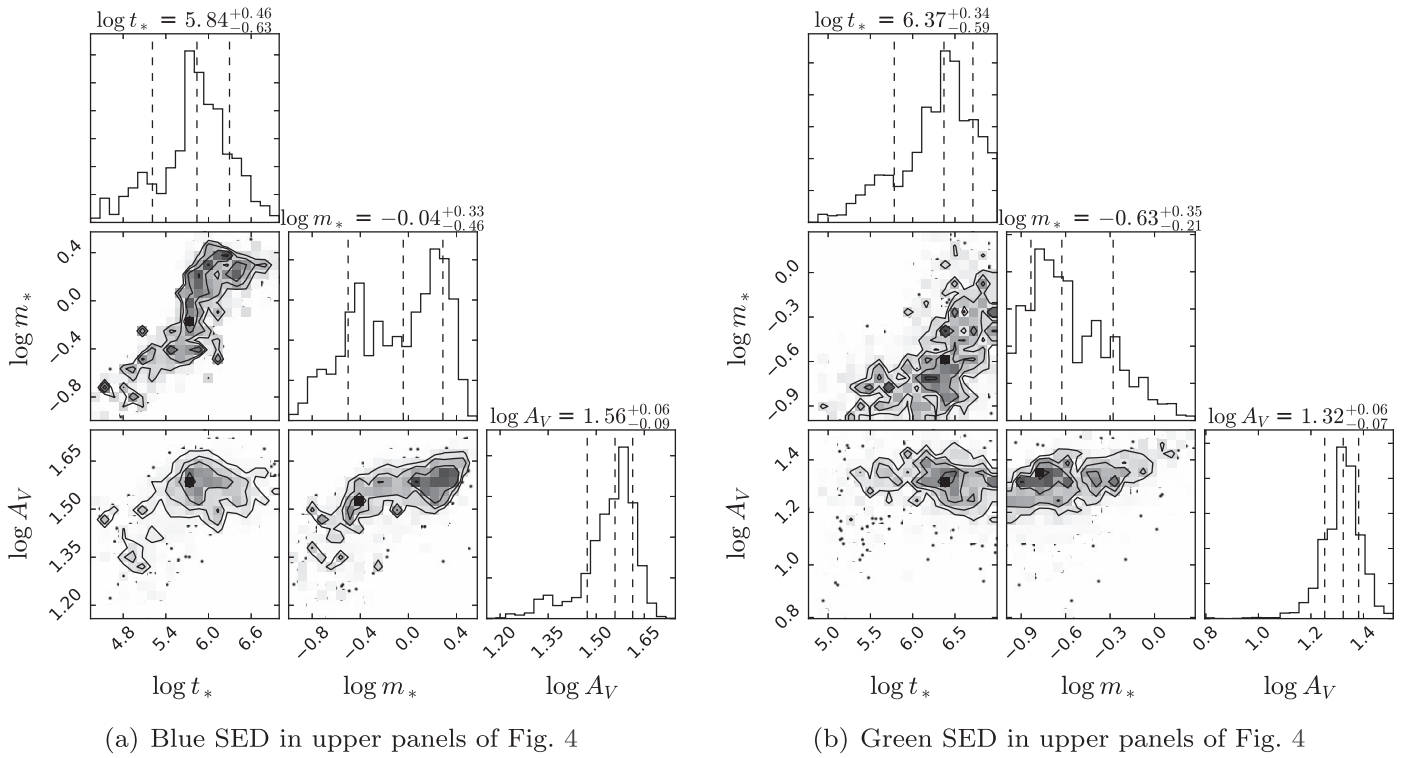


Figure 6. Posterior probability distributions of the model parameters for all three sources in cluster 6307, labeled according to the color of their SED in the upper panels of Figure 4. These are the final posteriors after the resolved fluxes from the image analysis have been included for the IRAC bands. The gray scale matches the probability density, and the marginalized probabilities are also shown. Vertical dashed lines correspond to the 0.25, 0.5, and 0.75 quantiles.

located in a line of sight not too far away from that to 5476, but closer to us, at about 1 kpc from the point where the Scutum–Centaurus arm meets the galactic bar. The spatial distribution of visual extinctions is also shown in Figure 8. Cluster 360,

located on the near side of the 3 kpc arm, has the highest derived optical extinction ($A_V = 58$) and also neighbors ($0''53$) a millimetric compact source containing a maser (Caswell et al. 2010; Urquhart et al. 2013).

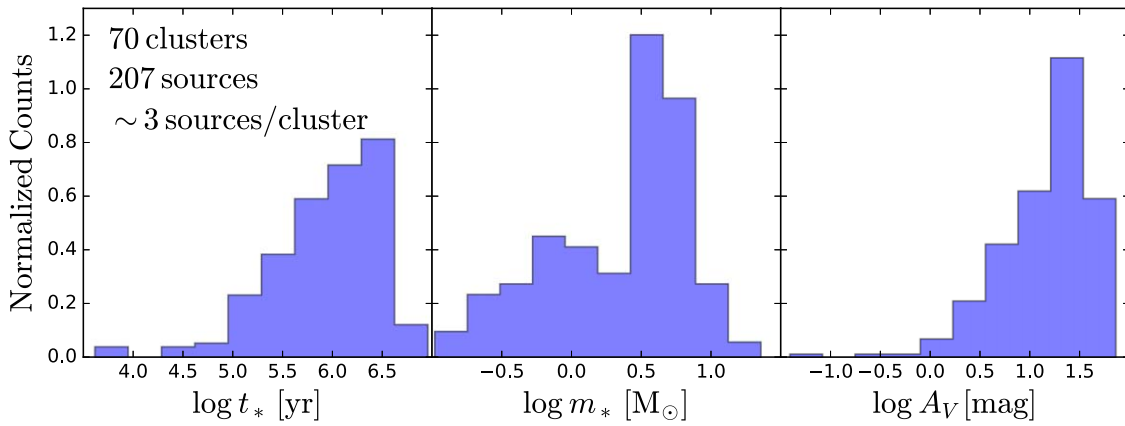


Figure 7. Histograms of source properties derived from the combined SED/image fitting. Shown are the 50% quantile values for YSO age, stellar mass, and visual extinction. All 207 individual YSOs making up the 70 clusters are used to generate these histograms.

4.2.3. Within-cluster Properties

Figure 9 illustrates the spatial distribution of mass and age dispersions within each cluster. The majority of clusters have small age dispersions, as measured by the difference between the ages of the oldest and the youngest stars ($t_{\max} < 2.5t_{\min}$), hinting at a relatively quick (although not necessarily coeval) formation of all detected members within the cluster. YSO age dispersion is less than a factor of 3 in 60% of the clusters, and more than a factor of 10 in only 13% of the cases. At least two clusters (4955 and 2568) show a significant age dispersion ($t_{\max} > 400t_{\min}$), but those are cases where a few relatively evolved sources (a few million years old or so) are in the same cluster with a single, considerably embedded Class I young source.

We searched for any existing correlations between the age of the oldest member in a given cluster (t_{\max}) and both the mass of its most massive member (m_{\max}) and the mass of its least massive star (m_{\min}). Figure 10 shows linear regression fits to these two correlations. Based on a p -value analysis, we find that at a 0.05 significance level, only the second of these two linear fits is significant enough to reject the null hypothesis with enough confidence. We will discuss the astrophysical implications of this correlation in Section 5.3, where we interpret it in terms of the cluster accretion history and the effect of dynamical evolution of the cluster in stopping this accretion. We note that the correlation holds across 1.5 orders of magnitude in t_{\max} , corresponding roughly to YSOs of classes II and III.

4.3. The $M_{\text{cl}} - m_{\max}$ Correlation

An important question in star formation is whether there is a nontrivial relationship between the total stellar mass of a cluster and the number and mass of its individual protostars, and, correspondingly, if and how the local IMF might be affected by such a nonlinearity. We attempt to shed light on the issue in the case of low-mass associations based on our results.

4.3.1. Corrected M_{cl}

Given a limiting flux below which faint sources are not detected, the completeness of clusters is a function of distance. Because the brightness of a source decreases as $1/d^2$, a star of a given luminosity is about 900 times fainter at a distance of 15 kpc (the distance to the most remote of our cluster) than it

would be at half a kiloparsec, and the fraction of the total cluster mass that remains undetected is therefore larger for more distant clusters. We therefore proceed to estimate a correction to M_{cl} for each cluster, based on their heliocentric distances.

In order to estimate this correction, we first note that it would be impractical to attempt to determine exactly how much mass is undetected for each cluster, because of the very nature of statistical sampling. However, we can obtain a reliable estimate and the associated uncertainties by looking at the typical properties of clusters of similar masses. A typical cluster in our sample has only one star more massive than $5 M_{\odot}$, with a few exceptional cases having a single star more massive than $10 M_{\odot}$. Using MC simulations, we randomly sampled 10^5 clusters containing a single $5 M_{\odot}$ star from a Kroupa IMF corrected for binarity, and we evaluated the typical number of members and total stellar masses of the resulting samples. We find that a cluster with a single star above $M_* = 5 M_{\odot}$ typically contains about 150 members and has a total stellar mass of $\sim 45 M_{\odot}$.

We then estimate the limiting mass at each heliocentric distance as the SED-derived mass of the least massive object detected in our sample within a small distance bin centered on the corresponding distance. We fit an exponential function to the resulting correlation and find that the limiting mass is $0.1 M_{\odot}$ at 1 kpc and $1 M_{\odot}$ at 10 kpc, with an uncertainty of 10% in logarithmic space. Using the MC simulation, we then estimate how much mass is typically contained below the limiting masses at each distance. Our results indicate that at 1 kpc we are missing between 4% and 8% of the cluster mass, whereas at 10 kpc this figure is between 45% and 55%. We use those values and their uncertainties to adjust a correction to $\log M_{\text{cl}}$ that scales linearly with $\log d$, and we apply this correction to the derived masses.

4.3.2. Derived Correlation and Mass–Luminosity Relationship

Figure 11 shows the resulting M_{cl} versus m_{\max} correlation for all 70 clusters studied here, all of which have five or fewer detected members with typical masses $m_* \sim 3 M_{\odot}$. The discussed correction to M_{cl} has been applied and contributes to the slope of this correlation according to $\Delta \log m_{\max} / \Delta \log M_{\text{cl}} = 0.14$, which is the difference in the best-fitting slope before and after the mass-completeness correction has been applied.

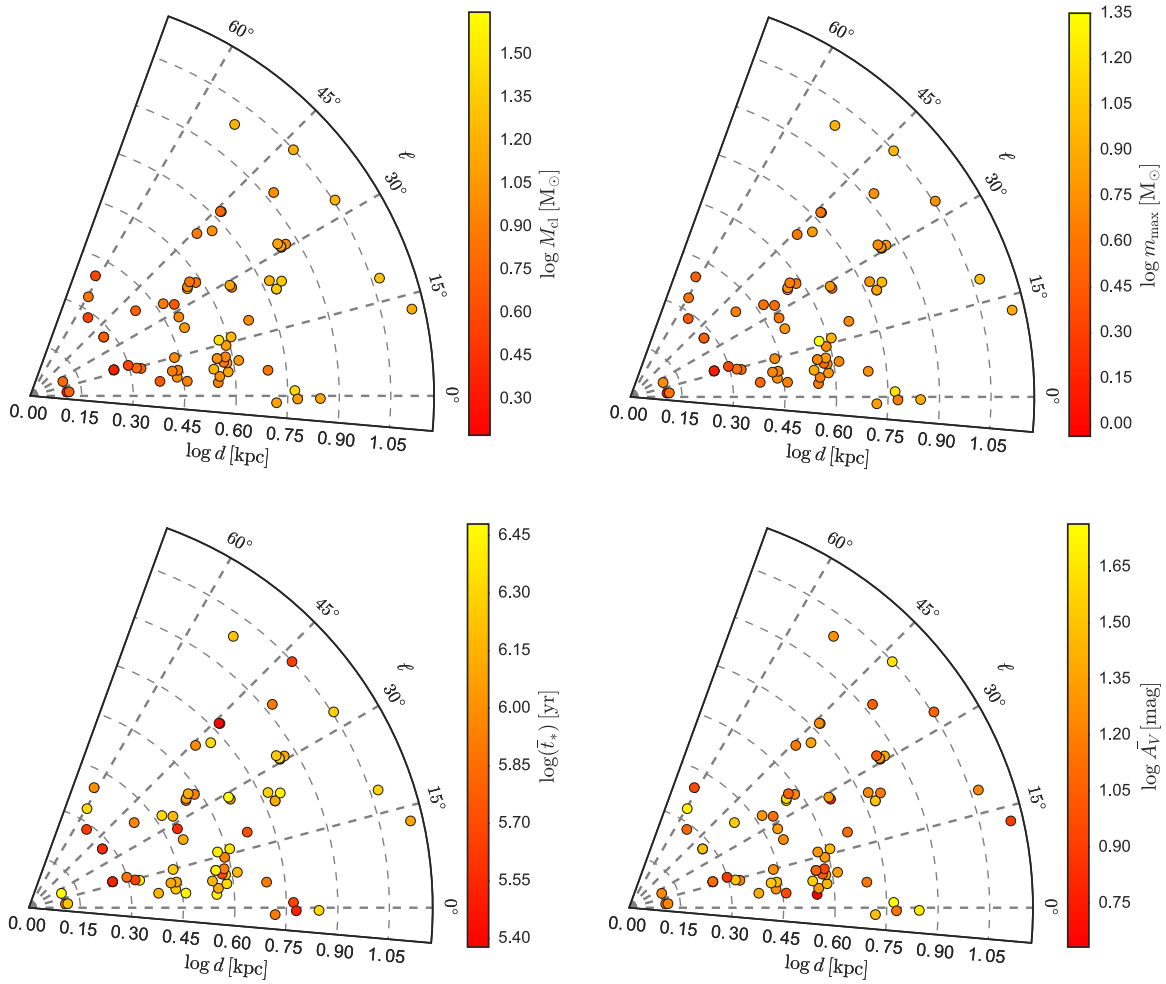


Figure 8. Projected locations of the studied clusters onto the galactic plane with colors indicating different derived properties. The upper two panels show the total stellar mass of the clusters and the mass of the most massive member in each of them. The lower two panels show the average ages and the average visual extinctions for each cluster. The grid is centered on the Sun.

For a given apparent brightness, $L_* \propto d^2$. We can use this expression in combination with the relationship between limiting mass and distance estimated above in order to estimate a mass–luminosity relation for the YSOs in our sample. Plugging the numbers, we get $L_* \propto m_*^{2.2}$. This derived mass–luminosity correlation is satisfactorily consistent with theoretical ideas like those of Myers (2012), who suggests a relation with a very similar exponent. However, the mass–luminosity relation for young stars is very much more uncertain than it is for stars dominated by nuclear burning processes or Kelvin–Helmholtz contraction, and we therefore do not claim that our results are necessarily a successful test of Myers (2012). However, the agreement between our results and their theoretical prediction increases the confidence in our results.

Accretion processes can dominate the luminosity of young stars and are functions of their mass and age, not to mention episodic periods determined by environmental considerations. The Myers (2012) relation, for example, is derived for protostars that are still accreting substantially, and of course the relation will also vary when the IMF varies from normal. All of these complexities, however, point to the potential value of our new method in comparative analysis of clusters. In future papers, we will explore larger samples to clarify the processes underway in clusters and help distinguish clusters,

ascertain more accurately their ages, and probe their IMFs and mass cutoffs.

4.3.3. Bayesian Linear Regression for the Correlation

We use a generalized linear model to perform Bayesian linear regression and estimate posterior distributions for the slope and the normalization of the resulting $M_{\text{cl}} - m_{\text{max}}$ correlation, and we compare these posteriors with theoretical predictions and previous empirical findings. In order to perform the statistical inference, we assume that each data point is sampled from a normal distribution $\mathcal{N}(\mu, \sigma)$. The correction applied to M_{cl} for each cluster, which itself has an uncertainty that has been accounted for, enters the fit as an additional error for this parameter, and therefore the posterior distributions resulting from Bayesian inference are consistent with all possible sources of error, to the best of our knowledge. We use uniform priors for both parameters.

The results of Bayesian linear regression are shown in Figure 12. The left panel shows the posterior for the slope compared to previous theoretical and semiempirical findings shown as the vertical lines. The right panel shows the posterior for the intercept compared with the same models. As for the scatter, we show in Figure 13 the distribution of the differences between $\log m_{\text{max}}$ and the mean of the distribution expected

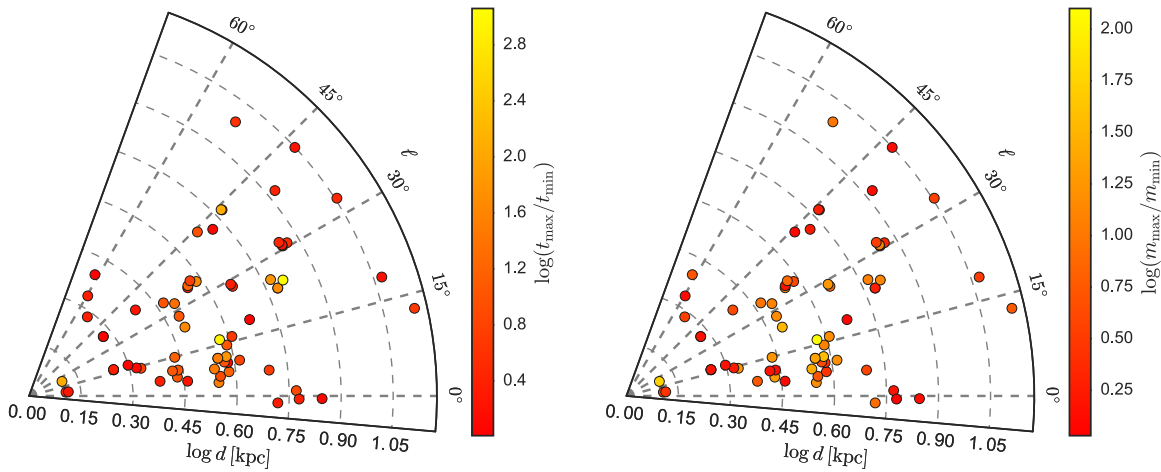


Figure 9. Projected locations of the studied clusters onto the galactic plane with colors indicating ranges of stellar ages (left panel) and masses (right panel). The color code indicates the ratio between the highest and lowest value of the individual components of the cluster in each case.

from our linear model. The Wilcoxon signed-rank test (Bhattacharyya & Johnson 1977) is used to determine whether this distribution is compatible with random sampling. According to the test, if the values have been sampled randomly from a symmetric distribution around the mean, then the percentage of measurements between the 1/6th and 5/6th quantiles should be around 66%. For the distribution of Figure 13, this percentage is 65.7%.

In both figures, the posteriors are compared to the following predictions for the $M_{\text{cl}} - m_{\text{max}}$ correlation:

1. *Salpeter IMF*: Elmegreen (2000) model distributions are constructed from a single-slope power-law Salpeter IMF; their combined luminosity exceeds the binding energy of the molecular cloud. The gravitational fate of the cluster is determined by the star formation efficiency, and the mass of the most massive star is set by the total number of stars, that is, random sampling applies, and the formation of isolated massive stars is possible (the double-dot-dashed correlation), in Figure 11.
2. *Empirical*: Larson (1982, 2003) models compare the properties of several molecular clouds with the stellar populations of the clusters within (the ρ Ophiucus cluster, the Orion Nebula cluster, the Quintuplet, and the R136 clusters) and derive the empirical relation shown as a dash-dotted line in Figure 11. The slope of this correlation (0.45) is shallower than what is predicted by a nominal Salpeter slope; according to the authors, this is the result of a lower star formation efficiency in the high-mass end due to feedback.
3. *Competitive accretion*: Bonnell et al. (2003) modeled stars in a young cluster accreting from a shared reservoir of gas. In gas-dominated regions of the cluster, usually in peripheral regions, the accretion is limited by tidal interactions, whereas in the cluster core the high relative velocities between stars results in Bondi–Hoyle accretion. The latter results in a fragmented IMF that is steeper for the high-mass stars that form in the cluster core with respect to the shallower IMF for low-mass stars that form in gas-dominated regions. This naturally results in the $M_{\text{cl}} - m_{\text{max}}$ correlation shown as the dotted line in Figure 11.
4. *Random sampling*: Oey & Clarke (2005) analytically derive the correlation between M_{cl} and m_{max} assuming

that the stars are randomly produced according to a Salpeter IMF. The correlation they obtain is shown as the long-dashed line in Figure 11. Their study, which includes results for a sample of young, nearby OB associations, concludes that there is a fundamental upper mass limit that truncates the IMF and estimates a very low probability for optimal sampling that depends on the cluster mass.

5. *Analytic random sampling*: Weidner & Kroupa (2004) assume in their study that a fundamental upper mass limit exists at $m_{\text{max}} = 150 M_{\odot}$ and use the canonical multipart Kroupa IMF to find the correlation shown as the short-and-long-dashed line in Figure 11.

5. Discussion

In this section, we explore how the physical properties we derive for individual YSOs in low-mass ($M_{\text{cl}} < 100 M_{\odot}$) clusters reflect the physical processes of star formation in individual clusters of various morphological types.

5.1. Construction of the IMF for Low-mass Clusters

Are all the stellar masses in the galaxy produced via a single universal IMF, or does the distribution of masses depend on the environment, making the integrated IGIMF of stars different from the canonical IMF? (The IGIMF is usually discussed in the context of massive stars, but here we consider it in its broadest sense.) If the IMF results from a random sampling process in any given cluster, then star formation is agnostic to the conditions of the environment, including the total mass of the birth cluster; no self-regulation is at play. If, on the other hand, the stellar masses in a cluster are preferentially determined starting with the most massive of its members, then this implies that star formation is self-regulated, and that the mass of the most massive star depends on the available resources in the cluster.

The results from Figures 11–13 allow us to probe some of the questions initially posed about the IMF, at least for our sample of clusters with masses below $100 M_{\odot}$. They indicate that the $M_{\text{cl}} - m_{\text{max}}$ correlation is already present in this regime of low-mass clusters, and that it is incompatible with simple assumptions of a power law of slope 1. When the intercept and the slope of the correlation are considered together, the

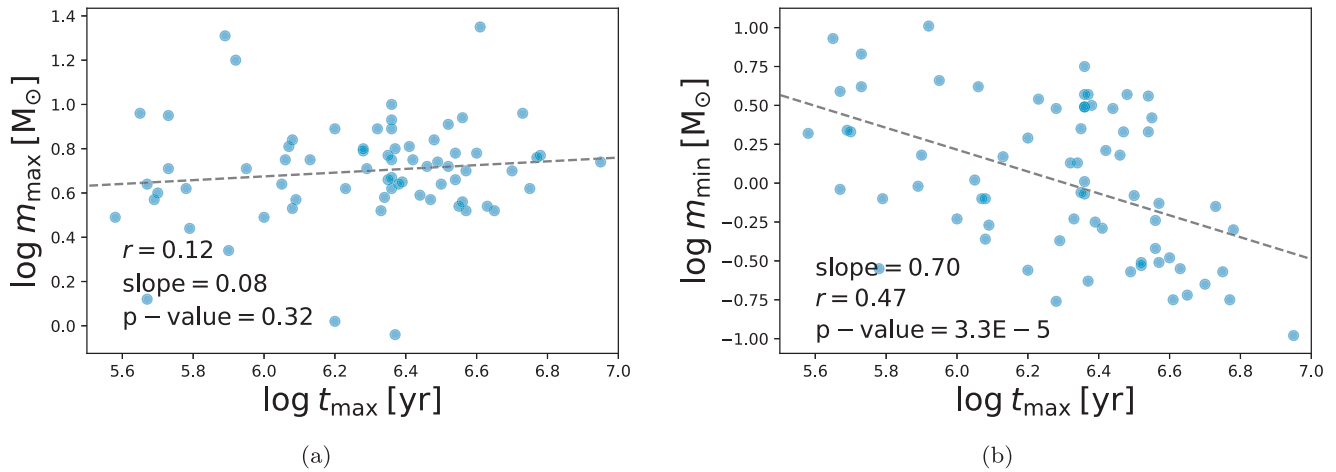


Figure 10. Relationship between the age of the oldest member in each cluster and (a) the most massive member and (b) the least massive member. The dotted lines are linear fits to the data, with parameters of the fit indicated.

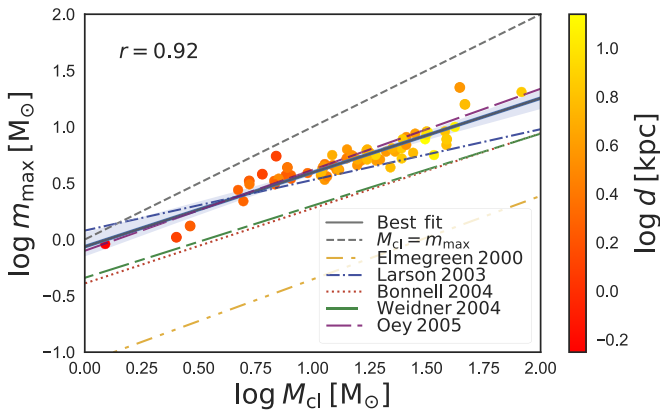


Figure 11. Mass of the most massive cluster member as a function of the cluster mass. The dots are the point estimates from the MCMC sampling and are color coded by cluster distance. The solid line corresponds to the best fit using Bayesian linear regression, and the shaded blue area is the 1σ credible interval. Also shown with different line styles are the theoretical and semiempirical predictions discussed in Section 4.3. The r value of the linear fit is also indicated.

posterior distributions for the correlation parameters are most compatible with the Oey & Clarke (2005) analytical model that assumes a fundamental high-mass limit for stellar objects and results in a truncated IMF. The distribution of m_{\max} values around the mean of the distribution expected from the linear model is compatible with random sampling from that model, according to the Wilcoxon signed-rank test.

This paper only samples clusters up to masses of $100 M_{\odot}$ and does not address the upper mass limit possible in a normal IMF. We can speculate, however, on whether it is likely that the results in Figure 11 might extrapolate to larger mass clusters. If it did, then the limit found by Oey & Clarke (2005) of $120\text{--}200 M_{\odot}$ (although it is not very well determined) would be reached in clusters of $M_{\text{cl}} \sim 5000 M_{\odot}$. Other authors have made attempts to set a more specific limit, such as the Weidner & Kroupa (2004) study, which also assumes random sampling, but with a clear upper limit at $m_{\text{upper}} = 150 M_{\odot}$. This would affect the normalization of the $M_{\text{cl}} - m_{\max}$ correlation, and our data for relatively lower mass clusters appear to be incompatible with that specific upper mass limit, as the normalization is significantly off from this prediction.

In conclusion, our results show that random sampling of a truncated IMF is the process most compatible with the observational evidence, at least in the cluster mass range considered here, and that no significant suppression of high- or medium-mass stars occurs within the considered range of cluster masses. On the other hand, our results do not rule out optimal sampling at larger cluster masses; competitive accretion, therefore, as a physical driving process remains a plausible model for the formation of low-mass clusters as well. More work is needed to determine if the star formation processes allow feedback mechanisms to dominate in larger clusters in a way that is ineffective in the smaller ones we consider here. Whatever the precise shape of the $M_{\text{cl}} - m_{\max}$ curve at high M_{cl} , it is clear that as more massive stars are formed in more massive clusters, a much stronger radiation field is present, more violent outflows are probable, and shorter evolutionary timescales may overwhelm the effectiveness of slow processes.

We confirm previous studies by Maschberger & Clarke (2008) and Weidner et al. (2010), both of which conclude that no suppression of high stellar masses can be inferred in clusters below the $100 M_{\odot}$ limit, and that the distributions of stellar masses in these clusters are compatible with random sampling. However, our results do impose useful constraints on the possible mass distributions of clusters below the $100 M_{\odot}$ limit. Our results imply that individual stellar masses in galactic clusters with masses below $100 M_{\odot}$ are statistically determined at random from a Kroupa IMF. We find that stars with masses $m_{*} > 5 M_{\odot}$ can be formed in clusters containing of the order of 150 members and having total stellar masses $M_{\text{cl}} = 45 M_{\odot}$. The occurrence of such medium-mass stars in low-mass clusters is both consistent with random sampling and confirmed observationally in our sample of low-mass clusters.

5.2. Implications for Competing Theories of Star Formation

Competitive accretion is not ruled out for low-mass stars, according to our above analysis and given the uncertainties, but it is unlikely to affect the IMF of low-mass clusters significantly. The theory of competitive accretion (Bonnell et al. 2004) results in optimal sampling and predicts a slope of the $M_{\text{cl}} - m_{\max}$ correlation within 1σ of our measured slope and an intercept within 3σ of our measured value. However, the competition for a limited reservoir of gas as envisioned in this

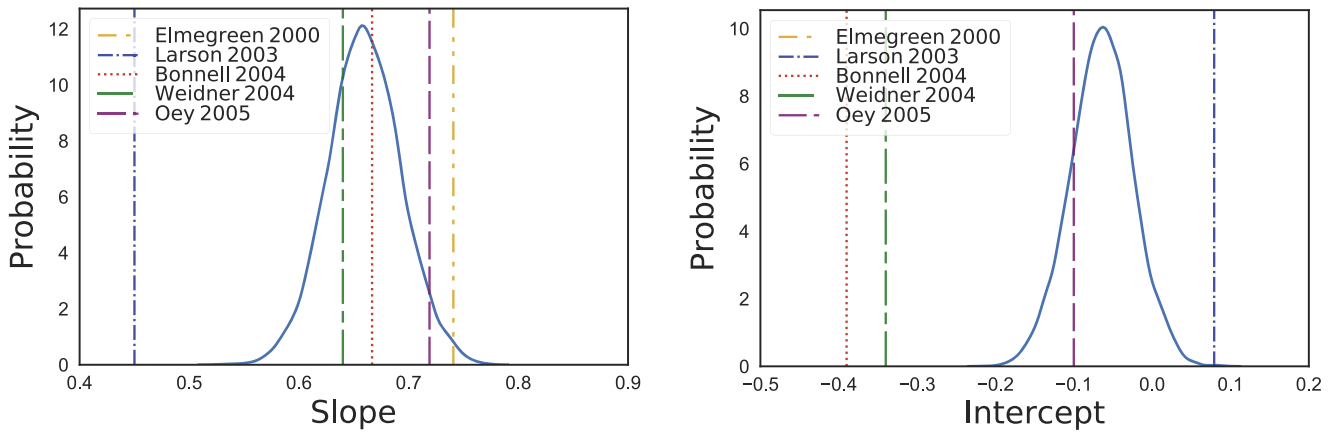


Figure 12. Posterior distributions for the slope (left) and intercept (right) of the $M_{\text{cl}} - m_{\text{max}}$ correlation as derived from Bayesian linear regression, compared with the values predicted by several theoretical end empirical studies (vertical lines). The blue solid line is the posterior measured from the data.

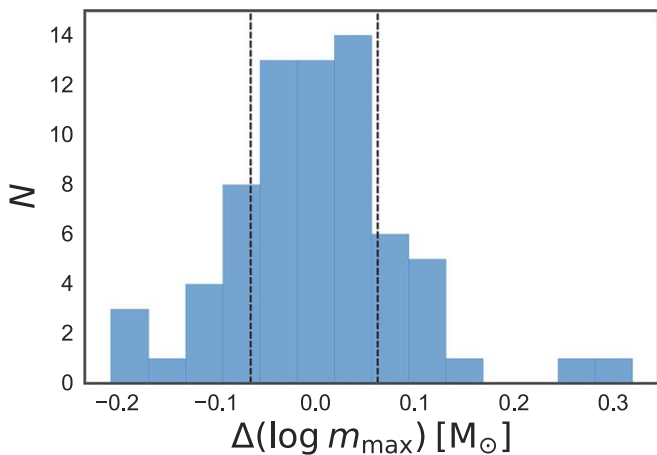


Figure 13. Distribution of $\log m_{\text{max}}$ values around the mean expected from our linear model. The vertical lines indicate the 1/6th and 5/6th quantiles.

model is more likely to take place in more massive clusters than those studied here. We can, nevertheless, rule out some of the proposed models of star formation for low-mass clusters.

The empirical correlation found by Larson (2003) that holds for more massive clusters such as the ρ Ophiuchus cluster, the Orion Nebula cluster, and R136 breaks down for low-mass clusters. This correlation results from an increasing difficulty in forming progressively more massive stars due to the effects of radiation pressure and winds, and it translates into a steeper IMF than the one observed in the present work. At the mass range studied here, however, the IMF appears to be self-similar, implying that radiation effects in low-mass clusters do not prevent the formation of the most massive stars allowed by the IMF. Likewise, the Elmegreen (2000) model, which assumes a dominant role for gravity in limiting growth, is excluded by our results.

Consistency between the observed photometry and the models informs the mode of star formation. For example, the spherical geometries with accreting material assumed by the Robitaille SED models are consistent with monolithic collapse (McKee & Tan 2003), but inconsistent with the stellar merger model (Bonnell et al. 1998), according to which massive stars do not form via accretion, but rather as the result of mergers of smaller stars. Also, if competitive accretion were the preferred mode of SF in the Milky Way, we would expect to see many more clusters than isolated single cores, and the

luminosity of the cluster members should depend on their location with respect to the gravitational potential of the cluster. *Consistency* is not the same as *proof*, however, so our results are most valuable from a statistical point of view and in providing a robust starting point for more detailed modeling.

5.3. Dynamical Stopping of Accretion and the IMF

Radiation hydrodynamical simulations have shown that in clustered environments, the IMF originates from competition between accretion and the dynamical interactions that terminate this accretion (Bate 2012). In these simulations, low-mass and high-mass stars form via the same process, but in the case of massive stars, the dynamical termination of the accretion occurs later. Building along these lines, Myers (2011) proposes a model for competitive accretion in the dense regions of young clusters. According to this model, which assumes a constant birth rate for the protostars as opposed to coeval birth, the maximum protostar luminosity in a cluster indicates the age and mass of its oldest accreting protostar. The distribution of protostar masses evolves in time as the least massive stars undergo early accretion and then stop while the massive stars continue accreting.

The significant correlation between t_{max} and m_{min} shown in the left panel of Figure 10 supports this accretion-driven, mass-evolving scenario: dynamical effects stop the accretion of individual stars, but the termination of accretion occurs later for massive stars. As the most massive stars in the cluster continue feeding from the surrounding gas and accretion has been terminated for stars of lower mass, the mass of the most massive star in the cluster continues to increase. But with a finite amount of gas available, longer accretion periods for the massive stars also mean shorter accretion periods for the low-mass stars, which explains the fact that the clusters that accrete for longer also have the lowest-mass protostars (see Figure 10(b)). This is consistent with the dynamical termination of the accretion scenario described in Bate (2012), which translates into a time evolution of the distribution of masses as accretion stops.

We interpret the lack of a significant correlation between t_{max} and m_{max} as being the result of most clusters being close to the final, time-independent mass distribution. Our hypothesis is that this is a stage in their evolution that lasts for a relatively long time, so our sample merely reflects this time-weighted distribution. The last YSOs still accreting are reaching the

dynamical termination of their accreting phases, and the mass distribution is settling down, resulting in a negligible increase of the maximum mass with age. This picture is consistent with the distribution of ages shown in Figure 7, with the majority of YSOs being older than 1 Myr.

5.4. Accelerating Star Formation and Cascade Fragmentation

We pointed out in Section 4.2.3 that at least two clusters, 4955 and 2568, contain highly embedded YSOs next to more evolved Class III objects. This association is not uncommon. In nearby embedded clusters such as the Serpens cloud core and NGC 1333, Winston et al. (2009) have reported a significant age spread of the YSO populations and report spatial segregation of young stars of different ages. Additionally, Willis et al. (2013) have shown that star formation in giant molecular clouds spatially progresses across regions, with younger, more embedded sources typically clustering in the central regions of the cluster. One possible scenario to explain age spreads of this magnitude is the accelerating star formation proposed in Huff & Stahler (2006) for the Orion Nebula cluster, according to which the parent cloud rapidly contracts before dissipating, creating an event of accelerated star formation. Contamination from field stars is less likely for the spatially compact clusters studied here, but cannot be completely ruled out. It is nevertheless hard to assess the validity of this theory with such a small sample.

Another scenario to consider here is the turbulent fragmentation cascade (Joncour et al. 2017), in which the initial fragmentation of a dense core into a wide pair will lead to further fragmentation of each of the members of the pair, the extent of which depends on the initial separation between both fragments. The physical size of practically all of the small clusters considered here is less than 0.15 pc, about the typical width of the interstellar filaments identified by *Herschel* (André et al. 2014). This implies that all members of a cluster can be associated with a single initial core within a filament. A significant fraction of the multiple systems in our sample are wide pairs, with separations larger than 10^4 au.

According to the fragmentation cascade scenario, it is likely that this wide configuration is an imprint of their spatial correlation at birth. Further fragmentation of the pair is predicted by the theory, and it is possible that fragmentation at smaller scales is not resolved by our NIR observations. This is something that we will be able to test with *JWST*. Meanwhile, our observations are consistent with these clusters being formed as the result of the fragmentation of a single initial core. Since protostellar multiplicity is higher than the multiplicity of field stars (Duchêne & Kraus 2013), suggesting that early dynamical evolution disrupts these young clusters, the ages derived by our analysis impose a lower limit on the cluster age at which this dynamical disruption ends. This age is of the order of the oldest individual age derived here, which is just below 10 Myr.

6. Conclusions

Most stars form in clusters, and studies of star formation processes are inhibited by the fact that individual sources are often blended in spatially unresolved young clusters. This long-standing problem in the study of YSOs has hindered our ability to characterize star formation processes more precisely, especially the population of fainter, lower mass stars in clusters

with massive siblings. In this paper, we offer a new Bayesian statistical method to address the issue. We analyze the infrared SEDs of a sample of 70 *Spitzer*-selected, low-mass ($M_{\text{cl}} < 100 M_{\odot}$) young clusters in the galactic plane whose individual members appear blended together within the *Spitzer* beam. The technique allows us to model the probable SEDs of individual YSOs using all available bands, including those where the cluster is spatially unresolved. Starting with prior information from the highest resolution images, our method estimates the most likely flux for each individual member in each band by sequentially fitting the unresolved SEDs and images, and for each individual YSO it recovers the posterior probability distributions for the fundamental physical parameters: stellar mass, evolutionary stage, and optical extinction.

The combined information obtained on individual YSO properties and the average properties of the low-mass clusters allow us to investigate how star formation proceeds in clustered environments containing tens of stars, and to assess whether the IMF is populated randomly in this mass range, or if self-regulating mechanisms lead to optimal sampling. Our main conclusions to date are based on a modest but representative sample of 70 clusters selected from *Spitzer* surveys and are aimed in part at illustrating the power of this method.

1. We have extracted the most probable photometry for YSO members of unresolved low-mass clusters across the galactic plane; more definitive measurements would require higher spatial resolution than is available. We present the method and compare the results against a variety of theoretical simulated scenarios. The method is very general and can be applied to young protostellar clusters with even larger-beam, longer-wavelength data sets, including *WISE* and *Herschel*. The FIR measurements in particular can also constrain the total dust masses and temperatures of the clusters. The predictions will soon be testable using the observational capabilities of *JWST*.
2. For clusters with total stellar masses below $100 M_{\odot}$, the distribution of stellar masses within the clusters and its relation to M_{cl} are indistinguishable from a randomly sampled, truncated Kroupa IMF. Therefore, any effects of self-regulated star formation that affect the IMF sampling significantly enough to alter the shape of the $M_{\text{cl}} - m_{\text{max}}$ correlation are likely to play a role only at larger cluster masses. This is perhaps not surprising as we expect the effects of self-regulation to be detectable in the much denser environments of massive $M_{\text{cl}} > 10^3 M_{\odot}$ clusters.
3. Random sampling of the IMF in low-mass clusters is able to produce intermediate-mass stars ($m_{*} \sim 5 M_{\odot}$) in clusters with only 150 members that have total stellar $M_{\text{cl}} \sim 45 M_{\odot}$.
4. The age of the oldest star is anticorrelated with the mass of its least massive star. This supports the putative effects of dynamical stopping in an accretion scenario, as derived from several smoothed particle hydrodynamics simulations. In this scenario, low-mass and high-mass stars form via the same accretion mechanism, but the dynamical termination of accretion occurs later in the case of massive stars, which therefore end up accreting for longer times.
5. Stellar mass growth due to accretion in stars that are born at a constant rate produces a time-dependent distribution of stellar masses. This distribution evolves as the least

massive stars undergo an early termination of accretion while the massive stars continue accreting for longer times. When accretion stops for these massive stars, an equilibrium distribution is reached. Our results indicate that in clusters with masses below $100 M_{\odot}$, this equilibrium distribution is reached when the cluster age reaches 1 Myr.

6. The masses of all clusters studied here are compatible with their having formed from the fragmentation of a large core in a molecular filament. For those systems that are binary, cascade fragmentation suggests that multiplicity can increase at smaller scales, beyond our resolution limit. *JWST* will be able to test this hypothesis in detail.
7. Using SED fitting, we have identified two sites of early massive star formation in the vicinity of maser emission sources. These sources contain some of the most embedded YSOs in our sample and are located on opposite sites of the 3 kpc arm.

The authors are grateful to the referee for very insightful comments that have improved this paper. The authors would like to acknowledge partial support from NASA grants NNX12AI55G and NNX10AD68G for the successful completion of this work. We would also like to thank Phil Myers and Lynn Carlson for a critical reading of the manuscript. Some of the calculations for the present work were done using the Odyssey cluster at Harvard University's Faculty of Arts & Sciences.

ORCID iDs

J. Rafael Martínez-Galarza  <https://orcid.org/0000-0002-5069-0324>

References

- André, P., Di Francesco, J., Ward-Thompson, D., et al. 2014, in *Protostars and Planets VI*, ed. H. Beuther et al. (Tucson: Univ. Arizona Press), 27
- Azimlu, M., Martínez-Galarza, J. R., & Muench, A. A. 2015, *AJ*, 150, 95
- Bastian, N., Covey, K. R., & Meyer, M. R. 2010, *ARA&A*, 48, 339
- Bate, M. R. 2012, *MNRAS*, 419, 3115
- Benjamin, R. A., Churchwell, E., Babler, B. L., et al. 2003, *PASP*, 115, 953
- Bhattacharyya, G. K., & Johnson, R. A. 1977, *Statistical Concepts and Methods* (New York: Wiley)
- Bonnell, I. A., Bate, M. R., Clarke, C. J., & Pringle, J. E. 2001, *MNRAS*, 323, 785
- Bonnell, I. A., Bate, M. R., & Vine, S. G. 2003, *MNRAS*, 343, 413
- Bonnell, I. A., Bate, M. R., & Zinnecker, H. 1998, *MNRAS*, 298, 93
- Bonnell, I. A., Vine, S. G., & Bate, M. R. 2004, *MNRAS*, 349, 735
- Bressert, E., Bastian, N., Gutermuth, R., et al. 2010, *MNRAS*, 409, L54
- Carey, S. J., Noriega-Crespo, A., Price, S. D., et al. 2005, *BAAS*, 37, 63.33
- Carlson, L. R., Sewilo, M., Meixner, M., Romita, K. A., & Lawton, B. 2012, *A&A*, 542, A66
- Caswell, J. L., Fuller, G. A., Green, J. A., et al. 2010, *MNRAS*, 404, 1029
- Chabrier, G. 2003, *PASP*, 115, 763
- Churchwell, E., Babler, B. L., Meade, M. R., et al. 2009, *PASP*, 121, 213
- Duchêne, G., & Kraus, A. 2013, *ARA&A*, 51, 269
- Elmegreen, B. G. 2000, *ApJ*, 539, 342
- Elmegreen, B. G., Klessen, R. S., & Wilson, C. D. 2008, *ApJ*, 681, 365
- Fazio, G. G., Hora, J. L., Allen, L. E., et al. 2004, *ApJS*, 154, 10
- Forbrich, J., Tappe, A., Robitaille, T., et al. 2010, *ApJ*, 716, 1453
- Green, G. M., Schlafly, E. F., Finkbeiner, D. P., et al. 2015, *ApJ*, 810, 25
- Guzmán, A. E., Sanhueza, P., Contreras, Y., et al. 2015, *ApJ*, 815, 130
- Hewett, P. C., Warren, S. J., Leggett, S. K., & Hodgkin, S. T. 2006, *MNRAS*, 367, 454
- Huff, E. M., & Stahler, S. W. 2006, *ApJ*, 644, 355
- Indebetouw, R., Mathis, J. S., Babler, B. L., et al. 2005, *ApJ*, 619, 931
- Indebetouw, R., Robitaille, T. P., Whitney, B. A., et al. 2007, *ApJ*, 666, 321
- Joncour, I., Duchêne, G., & Moraux, E. 2017, *A&A*, 599, A14
- Kroupa, P. 2001, *MNRAS*, 322, 231
- Kroupa, P., & Boily, C. M. 2002, *MNRAS*, 336, 1188
- Kroupa, P., & Weidner, C. 2003, *ApJ*, 598, 1076
- Kroupa, P., Weidner, C., Pflamm-Altenburg, J., et al. 2013, in *The Stellar and Sub-stellar Initial Mass Function of Simple and Composite Populations*, ed. T. D. Oswalt & G. Gilmore (Dordrecht: Springer), 115
- Lada, C. J., & Lada, E. A. 2003, *ARA&A*, 41, 57
- Larson, R. B. 1982, *MNRAS*, 200, 159
- Larson, R. B. 2003, in *ASP Conf. Ser. 287, Galactic Star Formation Across the Stellar Mass Spectrum*, ed. J. M. De Buizer & N. S. van der Bliik (San Francisco, CA: ASP), 65
- Lomax, O., & Whitworth, A. P. 2018, *MNRAS*, 475, 1696
- Lomax, O., Whitworth, A. P., Hubber, D. A., Stamatellos, D., & Walch, S. 2015, *MNRAS*, 447, 1550
- Maschberger, T., & Clarke, C. J. 2008, *MNRAS*, 391, 711
- McKee, C. F., & Tan, J. C. 2003, *ApJ*, 585, 850
- Morales, E. F. E., & Robitaille, T. P. 2017, *A&A*, 598, A136
- Morales, E. F. E., Wyrowski, F., Schuller, F., & Menten, K. M. 2013, *A&A*, 560, A76
- Mottram, J. C., Hoare, M. G., Urquhart, J. S., et al. 2011, *A&A*, 525, A149
- Myers, P. C. 2011, *ApJ*, 743, 98
- Myers, P. C. 2012, *ApJ*, 752, 9
- Oey, M. S., & Clarke, C. J. 2005, *ApJL*, 620, L43
- Robitaille, T. P. 2008, in *ASP Conf. Ser. 387, Massive Star Formation: Observations Confront Theory*, ed. H. Beuther, H. Linz, & T. Henning (San Francisco, CA: ASP), 290
- Robitaille, T. P., Meade, M. R., Babler, B. L., et al. 2008, *AJ*, 136, 2413
- Robitaille, T. P., Whitney, B. A., Indebetouw, R., Wood, K., & Denzmore, P. 2006, *ApJS*, 167, 256
- Simon, J. D., Bolatto, A. D., Whitney, B. A., et al. 2007, *ApJ*, 669, 327
- Stamatellos, D., & Whitworth, A. P. 2009, *MNRAS*, 392, 413
- Szymczak, M., Pillai, T., & Menten, K. M. 2005, *A&A*, 434, 613
- Tobin, J. J., Looney, L. W., Li, Z.-Y., et al. 2016, *ApJ*, 818, 73
- Urquhart, J. S., Moore, T. J. T., Schuller, F., et al. 2013, *MNRAS*, 431, 1752
- Weidner, C., & Kroupa, P. 2004, *MNRAS*, 348, 187
- Weidner, C., Kroupa, P., & Bonnell, I. A. D. 2010, *MNRAS*, 401, 275
- Weidner, C., Kroupa, P., & Pflamm-Altenburg, J. 2013, *MNRAS*, 434, 84
- Wienen, M., Wyrowski, F., Menten, K. M., et al. 2015, *A&A*, 579, A91
- Willis, S., Marengo, M., Allen, L., et al. 2013, *ApJ*, 778, 96
- Winston, E., Megeath, S. T., Wolk, S. J., et al. 2009, *AJ*, 137, 4777